Received: 17 May 2026 | Revised: 24 August 2026 | Accepted:19 October 2026| Published online: 27 November 2026

RESEARCH ARTICLE

Medinformatics
2026, Vol. 00(00) 1–24
DOI: 10.47852/bonviewMEDIN620210434

BON VIEW PUBLISHING

A Fuzzy Morphological Approach for Unsupervised Lung Infection Segmentation in Chest CT Images

Debasish Biswas[1], Shouvik Chakraborty[2,*] and Chinmoy Ghorai[1]

[1] *Department of Electronics and Telecommunication Engineering, Jadavpur University, India*

[2] *Department of Computer Science and Technology, Women's Polytechnic, India*

Abstract: Chest computed tomography (CT) is widely used to assess pulmonary abnormalities in COVID-19, but identifying infection regions is difficult without annotated data. We present an unsupervised pipeline that enhances and segments chest CT images with no training data. Classical thresholding methods such as Otsu's and Kapur's assume a fixed statistical criterion and a roughly bimodal histogram, an assumption that often breaks down in chest CT, where infected tissue blends gradually into normal lung parenchyma. Our framework instead couples two stages: fuzzy histogram equalization redistributes contrast across data-driven sub-histograms, and a morphological, area-gradient threshold reads its cut-point from that same enhanced histogram, so segmentation adapts to the contrast structure the enhancement actually produced. We evaluated the pipeline on ten publicly available chest CT images with COVID-19-related abnormalities from the COVID-19 CT Lung and Infection Segmentation Dataset. Enhancement improved the visibility of subtle radiological patterns, and segmentation delineated regions consistent with the combined ground-glass-opacity/consolidation "infection" category used in the reference masks. Against expert annotations, the method reached a Dice coefficient of 0.91 and an intersection over union (IoU) of 0.88, with an enhancement-stage peak signal-to-noise ratio of 19.43 dB and structural similarity index of 0.915, comparing favorably with recent supervised deep-learning methods evaluated under different protocols, despite needing no training data, no gradient-based optimization, and one fixed parameter set applied uniformly across all images; given the small evaluation set, this is indicative rather than a controlled benchmark. The framework's simplicity, low cost, and transparent processing suggest it may help preliminary CT assessment where data and computation are scarce.

Keywords: COVID-19, CT image analysis, fuzzy histogram, unsupervised segmentation, morphological filtering

1. Introduction

Chest computed tomography (CT) shows lung anatomy and tissue abnormalities in enough detail that it has become a standard tool for assessing respiratory disease. During the COVID-19 pandemic, clinicians used CT scans alongside RT-PCR to gauge how far pulmonary involvement had progressed and to track disease over time, since ground-glass opacities, bilateral infiltrates, and consolidation are all visible on a scan. None of these patterns is unique to COVID-19, though—the same opacities and consolidation turn up in other viral and bacterial pneumonias, organizing pneumonia, and pulmonary edema. So CT findings describe and quantify lung abnormality rather than pin down a specific cause; a definitive COVID-19 diagnosis still needs RT-PCR or another virological test alongside the clinical picture. Imaging nonetheless remains useful when a fast read is needed, which is the role it plays here—the computational framework we describe has not itself been validated in a clinical setting (see Limitations).

One of the main challenges in CT image analysis is the separation of abnormal lung regions from surrounding healthy tissue. Reliable segmentation is important for disease assessment, treatment monitoring, and computer-aided diagnostic applications. In recent years, deep learning methods have shown promising performance in this area. Architectures based on convolutional neural networks (CNNs), including U-Net, ResNet, and their variants, have been widely adopted for lesion detection and segmentation tasks [1, 2]. However, the effectiveness of these approaches depends heavily on the availability of large collections of accurately annotated images. Preparing such datasets requires considerable effort from experienced radiologists and is often impractical in situations where imaging resources or expert annotations are limited. The dependence on labeled data has encouraged the investigation of alternative segmentation strategies that can operate with minimal human intervention.

A variety of unsupervised techniques have been explored, including clustering-based methods, region-growing approaches, entropy-driven thresholding schemes, and morphology-oriented image analysis. These methods avoid the need for training data and are generally easier to implement and interpret than complex

***Corresponding author:** Shouvik Chakraborty, Department of Computer Science and Technology, Women's Polytechnic, Chandernagore, India. Email: shouvikchakraborty@wbscte.ac.in

© The Author(s) 2026. Published by BON VIEW PUBLISHING PTE. LTD. This is an open access article under the CC BY License (https://creativecommons.org/licenses/by/4.0/).

learning-based systems. More recent unsupervised approaches specific to COVID-19 CT analysis include Kapur entropy-based multilevel thresholding for automatic infection region segmentation and volumetric measurement [3], unsupervised domain adaptation for cross-domain infection segmentation without target-domain annotations [4], and fast domain-inspired unsupervised severity scoring directly from lung CT [5]. These studies indicate continued and recent interest in annotation-free approaches to COVID-19 CT analysis, motivating further development of unsupervised enhancement-segmentation frameworks such as the one proposed here. Among the general class of unsupervised methods, fuzzy logic–based techniques have attracted attention because they can represent uncertainty in image intensities more effectively than conventional deterministic models [6, 7]. This characteristic is particularly relevant for medical images, where tissue boundaries are often gradual and affected by noise, acquisition conditions, and patient-specific variations.

Morphological image processing has also been applied successfully to segmentation problems involving anatomical structures and pathological regions. By exploiting shape, connectivity, and spatial relationships among pixels, morphological operations can identify meaningful structures that may not be evident from intensity information alone. Several studies have combined fuzzy concepts with morphological analysis to improve segmentation robustness while maintaining relatively low computational complexity. Prior work combining fuzzy logic with morphological analysis has typically applied fuzzy techniques at the pixel-classification stage—for example, fuzzy c-means clustering used to delineate lung tumor or lung parenchyma regions—with morphological operations applied afterward as an independent postprocessing or reconstruction step [8, 9]. In these approaches, the fuzzy and morphological components are optimized separately and do not share a common intermediate representation. In contrast, the present framework applies fuzzy representation at the histogram-construction stage itself, using it to drive an adaptive, image-specific partitioning of the intensity range; the subsequent morphological, area-gradient-based threshold selection then operates directly on this partitioned, enhanced histogram, rather than as an independently tuned post-processing step applied to an already-classified image. Such approaches are attractive for clinical environments where fast processing and algorithm transparency are desirable.

Recent work has continued to explore contrast enhancement and lung imaging approaches adjacent to the present task, including a global-local hybrid CLAHE approach for X-ray image enhancement [10] and a GAN-based pipeline for 3D lung tumor reconstruction incorporating a lung segmentation stage [11].

Despite the progress reported in the literature, many unsupervised methods remain sensitive to variations in image contrast and intensity distribution. Differences in acquisition protocols, scanner settings, and patient characteristics can significantly influence segmentation performance. For chest CT images, these variations may obscure subtle pathological patterns and complicate the identification of infected regions. Improving image quality before segmentation therefore remains an important consideration. Two specific limitations in the existing unsupervised literature motivate the present work. First, classical unsupervised thresholding techniques—including Otsu's method, Kapur entropy maximization, and related global thresholding schemes—select a segmentation threshold based on a fixed statistical criterion (e.g., between-class variance or histogram entropy) that implicitly assumes a particular histogram shape, typically bimodality between foreground and background intensity classes. This assumption is frequently violated in chest CT images, where infection-related tissue exhibits a gradual, overlapping intensity transition with normal lung parenchyma rather than a clearly separable bimodal distribution, making a fixed statistical criterion an unreliable basis for threshold selection. Second, enhancement and segmentation are typically treated as independent, sequentially applied stages in existing unsupervised pipelines: an enhancement method improves image contrast without reference to how the subsequent segmentation stage will threshold the result, and the segmentation stage in turn applies a generic threshold-selection criterion without reference to the specific contrast redistribution the enhancement stage introduced. This decoupling means that even when enhancement successfully improves visual contrast, the segmentation stage may not exploit that improvement effectively. The present work addresses both limitations by coupling the two stages: the enhancement stage partitions the fuzzy histogram into data-driven subregions based on the image's own intensity distribution, and the segmentation stage derives its threshold from the area-gradient of that same enhanced image, rather than from a fixed, independently applied statistical criterion.

The use of an unsupervised approach in this work is motivated by three specific considerations relative to supervised and semi-supervised alternatives. First, annotation requirements: supervised methods such as U-Net-based architectures require pixel-level expert-annotated training data, which is costly to produce, requires radiologist time, and may be scarce or unavailable during the early phase of an emerging disease outbreak—precisely the setting in which rapid image analysis tools are most needed. The proposed method requires no training data or annotations of any kind. Second, computational cost: training a deep convolutional segmentation network typically requires GPU acceleration and hours to days of training time, in addition to inference-time computation. In contrast, the proposed pipeline consists of histogram computation, Gaussian smoothing, and morphological operations, requiring no training phase; a reference implementation processes a single CT slice in approximately 70 ms on a single CPU core, without GPU acceleration (runtime measured using a Python reference implementation of the described algorithm; actual performance may vary depending on implementation and hardware). Third, interpretability: each stage of the proposed pipeline—histogram partitioning, dynamic range allocation, and area-gradient threshold selection—operates on an inspectable, directly visualizable intermediate representation (the histogram, its derivative, and the resulting threshold curve), allowing a practitioner to examine why a particular threshold or enhancement was selected. This contrasts with deep learning models, whose internal representations are comparatively difficult to inspect or explain to a clinical end user without additional interpretability tooling, which itself provides only an approximate post hoc explanation rather than a direct account of the decision process [12].

The main objective of this work is to develop an unsupervised CT image analysis framework that addresses the two limitations identified above: the reliance of classical unsupervised segmentation on fixed statistical thresholding criteria, and the decoupling of enhancement and segmentation as independently optimized stages. The specific contributions of this study are as follows: (1) a fuzzy histogram enhancement stage that adaptively partitions and redistributes the intensity range based on the image's own histogram structure, rather than applying a globally fixed transformation; (2) a morphology-based, area-gradient segmentation stage whose threshold is derived directly from the enhanced image produced by stage (1), coupling the two stages through a shared intermediate representation; (3) a quantitative

evaluation against expert-annotated reference masks and comparison with both reimplemented classical unsupervised methods and standard global thresholding techniques (Otsu, Kapur, Yen, Triangle, Kittler–Illingworth), applied under matched conditions; and (4) an extensive sensitivity analysis of the framework's design parameters—including the enhancement kernel size and standard deviation, the fuzzy membership bandwidth, the peak-detection run-length criterion, and alternative peak-detection strategies—establishing that the reported results are not dependent on narrowly tuned parameter choices. Unlike supervised approaches, the proposed methodology requires no annotated training data and no gradient-based model optimization: a single fixed set of parameter values is applied uniformly across all ten evaluation images, without per-image tuning, retraining, or fine-tuning at inference time. This distinguishes the proposed framework from supervised methods, which require an annotation-dependent training procedure to fit model weights. It does not imply that the framework's design parameters (Section 2) required no empirical selection during development; as disclosed in Section 2, the Gaussian smoothing standard deviation was selected via inspection of enhancement results, and its robustness across a broad parameter range was subsequently verified (Table 1). The distinction is between one-time, design-stage parameter selection—common to essentially all image-processing pipelines, including classical thresholding methods such as Otsu's and Kapur's—and the data-driven, iterative training process required by supervised learning models, which the proposed framework does not require.

2. Materials and Methods

The segmentation stage identifies pulmonary infection regions, defined here as the combined extent of ground-glass opacity and consolidation, consistent with the "infection" annotation category used in the reference dataset (Section 3.1). The proposed method does not distinguish between ground-glass opacity and consolidation as separate classes; both are captured within a single binary infection mask, matching the granularity of the expert-annotated reference used for evaluation. The quality of chest CT images can be affected by low contrast, noise, and variations in intensity distribution, which may reduce the visibility of clinically important structures. The target of the segmentation stage is defined as follows: infection regions, encompassing ground-glass opacity and consolidation as a single combined class, consistent with the annotation category of the reference dataset used for evaluation (Section 3.1). Operationally, the segmentation stage identifies regions of increased pixel intensity within the extracted lung field (Section 2, lung-field extraction) following enhancement, using the area-gradient threshold criterion (Equation (14)–(16)). This criterion is intensity-based and does not incorporate explicit anatomical priors distinguishing infection regions from other structures of comparably increased density, such as pulmonary vasculature and bronchial walls; the segmented output should therefore be understood as an intensity-defined region of increased density within the lung field, which is expected to substantially overlap with, but is not guaranteed to be limited to, infection regions as defined above. Quantitative correspondence with expert-annotated infection regions is reported in Table 6. The framework's enhancement stage is built around a fuzzy histogram equalization step, which accounts for the uncertainty in pixel intensities that acquisition conditions, tissue heterogeneity, and imaging noise all introduce into medical images. Conventional histogram equalization puts each pixel into exactly one gray-level bin; here, a pixel instead contributes to several neighboring intensity levels according to a membership function, which smooths out the intensity distribution and makes the enhancement step less sensitive to abrupt gray-level jumps. We then convolve the resulting fuzzy histogram with a Gaussian kernel before equalization, to suppress random fluctuations further.

After smoothing, the histogram is analyzed to identify dominant intensity peaks. These peaks are used to partition the gray-level distribution into several regions, each corresponding to a specific intensity interval. Instead of applying a single transformation to the entire image, contrast enhancement is performed independently within each region. This localized treatment allows subtle image details to be emphasized without introducing excessive contrast changes in unaffected areas. Such an approach is particularly useful for CT images in which lesions, ground-glass opacities, and other infection-related patterns occupy only a limited portion of the available intensity range [13].

For each partition, the dynamic range is adaptively redistributed to improve local contrast. The resulting transformation function is derived from the fuzzy intensity distribution, where gray levels are represented by weighted membership values rather than discrete counts. Once the equalization process is completed, a brightness adjustment step is applied to preserve the overall luminance characteristics of the original image. Maintaining brightness consistency is important because excessive intensity shifts may alter the visual appearance of anatomical structures and complicate clinical interpretation. The enhancement procedure therefore seeks to improve visibility while retaining the natural characteristics of the CT scan [14, 15].

Global histogram equalization methods have long been used for image enhancement; however, they often produce unsatisfactory results when applied to images with uneven or restricted intensity distributions [16]. Several modifications have been proposed to improve brightness preservation and contrast control [16], yet many of these techniques continue to rely on conventional histogram representations in which intensity values are treated as precise and deterministic quantities [17, 18]. Such assumptions

Table 1. Sensitivity of enhancement-stage output quality (PSNR, SSIM) and downstream segmentation output (lung-area fraction, self-consistency Dice) to the Gaussian smoothing kernel size and standard deviation (σ) used in Equation (6), evaluated across the full ten-image dataset

Kernel size	σ = 0.5	σ = 0.75	σ = 1.0318 (paper)	σ = 1.5	σ = 2.0
1 × 5	PSNR 19.21 / SSIM 0.914	19.21 / 0.914	19.42 / 0.915	19.55 / 0.916	19.51 / 0.915
1 × 7	19.21 / 0.914	19.21 / 0.914	19.42 / 0.915	19.60 / 0.916	19.58 / 0.917
1 × 9 (paper)	19.22 / 0.914	19.22 / 0.914	19.43 / 0.915	19.60 / 0.916	19.56 / 0.917
1 × 11	19.22 / 0.914	19.22 / 0.914	19.43 / 0.915	19.60 / 0.916	19.60 / 0.917
1 × 13	19.22 / 0.914	19.22 / 0.914	19.43 / 0.915	19.60 / 0.916	19.60 / 0.917

may not accurately reflect the uncertainty present in medical imaging data. Variations arising from noise, partial-volume effects, and acquisition artifacts can cause neighboring tissues to exhibit overlapping intensity ranges, making rigid histogram representations less effective. To address this limitation, he proposed enhancement stage utilizes a fuzzy histogram in which pixel intensities are represented through graded membership values (Equation (3)), rather than the rigid, single-valued bin assignment of a conventional crisp histogram. The resulting histogram remains one-dimensional in gray level; membership is aggregated over the two-dimensional spatial domain of the image, but no additional contextual dimension (such as local gradient or local average intensity, as used in joint/bivariate histogram methods) is incorporated. The mathematical formulation of the fuzzy histogram employed in this study is given in Equation (3).

$$\sum_{k=0}^{L-1} h_k = S_1 \times S_2, \;\; h_k = \|(p,q); I(p,q) = k\| \tag{1}$$

In this equation, L denotes the count of the gray levels in the image I whose size is $S_1 \times S_2 \|.\|$ denotes the cardinality of the set. The probability of occurrence in the image matrix for each gray level can be computed using Equation (2).

$$prob_k = \frac{h_k}{S_1 \times S_2}, \;\; k = 0, 1, 2, 3, \ldots., L-1 \tag{2}$$

In CT imaging, pixel intensities are often affected by noise, acquisition conditions, and partial-volume effects, resulting in gradual transitions between adjacent tissues rather than sharply defined boundaries [19]. To account for these characteristics, the enhancement stage employs a fuzzy histogram representation. Instead of assigning each pixel exclusively to a single gray-level bin, the intensity contribution of a pixel is distributed among neighboring bins according to a membership function. The degree of membership ranges between 0 and 1 and reflects the association of a pixel with different intensity levels [20, 21]. This representation produces a smoother estimate of the gray-level distribution than a conventional histogram. As a result, local fluctuations caused by noise have less influence on the histogram profile, while subtle variations associated with anatomical structures remain preserved. In the implementation presented here, symmetric membership functions are used because they provide an effective compromise between computational cost and representation accuracy [22–24].

Enhancement-stage image quality was assessed using three measures: Mean squared error (MSE), peak signal-to-noise ratio (PSNR), and the structural similarity index (SSIM), computed between the original grayscale CT image and the enhanced grayscale image produced prior to thresholding (Equation (17)–(19)). MSE quantifies the average squared intensity difference between the two images; PSNR expresses this error relative to the maximum possible signal intensity, with higher values indicating greater fidelity; SSIM assesses structural similarity based on luminance, contrast, and spatial information, computed from local mean, standard deviation, and covariance (Equation (20)–(21)).

Segmentation accuracy was assessed against expert-annotated reference masks using the Dice similarity coefficient (DSC), Dice = $2|A \cap B| / (|A| + |B|)$, and IoU, IoU = $|A \cap B| / |A \cup B|$, where A denotes the predicted binary segmentation mask and B denotes the expert-annotated reference mask.

2.1. Preprocessing

Prior to enhancement, no CT windowing was applied by the present authors, as the source images were obtained as rendered grayscale case images (8-bit, 0–255 intensity range) from a public radiological case repository, in which windowing had already been applied by the contributing radiologist at the time of case publication. Consequently, the specific window/level settings used are not available to the present authors and are not independently controlled in this study; this is noted as a limitation in Section, since variation in source windowing across cases could contribute to the histogram variability observed in Figure 3.

Images were processed at their native resolution without resizing: eight of the ten images (axial views) had a resolution of 330 × 330 pixels, and the remaining two (coronal/sagittal views) had a resolution of 328 × 388 pixels (Section 3.1). No explicit resizing or resampling to a common resolution was performed, and the lung-field extraction, enhancement, and segmentation stages operate directly on each image's native pixel grid.

No dedicated image-domain denoising or noise-removal filter (e.g., Gaussian blur, median filtering, or non-local means) was applied to the CT images themselves. Noise suppression in the proposed framework instead occurs at two other points: (i) the Gaussian smoothing kernel (Equation (6)) is applied to the intensity histogram, not the image, to suppress spurious local extrema during peak detection; and (ii) morphological opening and closing operations (Section 2, lung-field extraction) remove small spurious connected components at the mask level. No pixel-domain intensity normalization (e.g., z-score standardization or explicit rescaling to a fixed range) is applied prior to enhancement; intensity rescaling occurs only as the final brightness-preservation step of the enhancement stage itself (Equation (13)), which corrects the output mean to match the input mean rather than normalizing the input.

All CT images in this study were analyzed as independent two-dimensional slices. No volumetric (3D) processing, inter-slice consistency enforcement, or 3D context was used at any stage of the proposed framework; each of the ten images was treated as a standalone 2D input.

Prior to enhancement, the lung parenchyma is isolated from each CT slice using the following pipeline:

1) Thresholding: Otsu's method is applied to the grayscale pixel intensities to separate air-equivalent (low-intensity) regions from soft tissue and bone. [Note: thresholding is performed on rendered grayscale intensity rather than Hounsfield Units, as the source images were obtained as rendered CT slices rather than raw DICOM data; where DICOM data with calibrated HU values are available, HU-based windowing (e.g., −1000 to − 500 HU for aerated lung) is a preferable and more standardized alternative.]
2) Border-connected component removal: components touching the image border—corresponding to background and the region outside the circular CT reconstruction field of view—are removed, since these share the same low-intensity range as lung air but are not anatomically part of the lung.
3) Morphological cleaning: binary opening (disk-shaped structuring element, radius 2) removes thin connections to vasculature and ribs; binary closing (radius 4) consolidates each lung into a single connected region.
4) Connected component selection: connected components are labeled, and the two largest components exceeding a minimum-area threshold (0.5% of image area, to discard

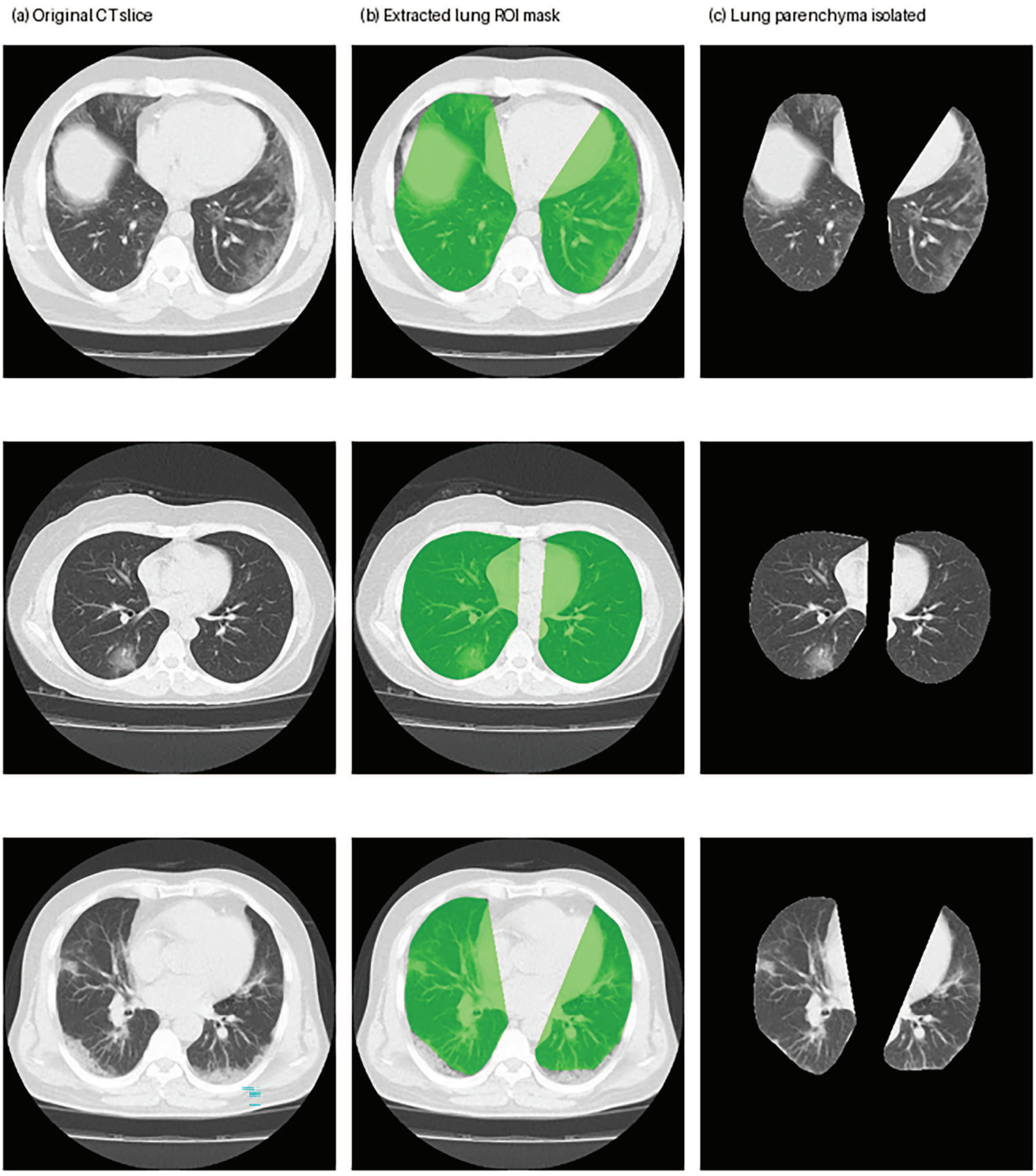

Figure 1. Lung-field ROI extraction prior to enhancement and segmentation. (a) Original CT slice. (b) Extracted lung mask (convex hull, green overlay). (c) Isolated lung parenchyma used as input to subsequent processing

residual noise specks) are retained as the left and right lung fields.

5) Convex hull recovery: because ground-glass opacity and consolidation regions are denser—and therefore brighter—than normally aerated lung, a strict low-intensity mask would exclude the pathological regions the framework is designed to detect. The convex hull of each retained lung component is computed, recovering interior higher-intensity pixels as part of the lung ROI.
6) Hole filling: residual small holes within the mask are filled, followed by a final light morphological closing (radius 3) for boundary smoothing.

The resulting binary mask defines the region over which the fuzzy histogram construction (Equation (3)) and area-gradient

thresholding (Equation (14)–(16)) are subsequently computed. Figure 5 shows representative examples across the dataset.

2.2. Parameter Sensitivity

To assess the sensitivity of the enhancement stage to the Gaussian smoothing kernel (Equation (6)), a parameter sweep was conducted over kernel sizes {5, 7, 9, 11, 13} and $\sigma \in \{0.5, 0.75, 1.0318, 1.5, 2.0\}$ across the full image set. PSNR varied by less than 0.4 dB and SSIM by less than 0.003 across the entire grid, and the final segmented lung-abnormality area was identical (Dice = 1.0 relative to the reported $\sigma = 1.0318$ setting) at every combination tested. This confirms that the reported parameter values were not arbitrarily selected to favor a particular outcome, and that the framework's segmentation output is robust to substantial variation in this preprocessing parameter. To determine whether the reported kernel size and standard deviation represent a robust design choice rather than an arbitrarily selected value, a sensitivity analysis was performed by systematically varying the kernel size ({5, 7, 9, 11, 13}) and σ (0.5 to 2.0) used in Equation (6), and evaluating the resulting change in enhancement quality (PSNR, SSIM) and final segmentation output across all ten images in the dataset. The results are summarized in Table 1 and illustrated in Figure 2.

Segmented lung-area fraction: 0.754 ± 0.05 across the full image set, identical at every kernel/σ setting tested (range 0.5–2.0, sizes 5–13). Self-consistency Dice between each setting's segmentation and the paper's own setting (9, 1.0318): 1.000 at every single point—the final binary segmentation output does not change at all across this parameter grid on ten images.

The bandwidth B was set to 2 based on a sensitivity check across $B \in \{1, 2, 3\}$ on the full image set (Table 2): enhancement quality changed only marginally (PSNR 19.16–19.66 dB, SSIM 0.914–0.916), and the resulting segmentation output remained highly consistent (Dice $\geq$ 0.989 relative to $B = 2$) across the tested range, indicating the framework is not sensitive to this parameter within a reasonable neighborhood size. $B = 2$ was retained as a moderate value that spreads membership across a small enough neighborhood to preserve gray-level resolution while still providing the smoothing benefit motivating the fuzzy formulation.

The fuzzy histogram also helps reduce discontinuities that frequently appear in CT intensity distributions. Such discontinuities may arise from quantization effects, acquisition artifacts, or variations introduced during image reconstruction. By allowing neighboring intensity levels to share information, the histogram profile becomes more continuous and better suited for subsequent enhancement operations. Examples of this variability across the dataset are shown together with the test images in Figure 3 [24]. Following the enhancement stage, the processed image is subjected to morphology-based segmentation. Threshold determination is performed using an area-analysis procedure derived from the image intensity distribution. For each candidate threshold, the cumulative proportion of pixels below that threshold is calculated, producing a monotonic area curve that reflects the overall distribution of gray levels within the image. To identify the most significant structural transition, the first derivative of the area curve is evaluated. This derivative, referred to as the morphological area gradient, highlights intensity levels at which substantial changes occur within the image. Because derivative-based measures can be affected by noise, the gradient curve is smoothed using a Gaussian filter prior to threshold selection. The threshold corresponding to the maximum gradient response is then selected as the operating point for segmentation. Once the threshold has been determined, a binary mask is generated to separate candidate abnormal regions from the surrounding lung tissue. Regions exhibiting imaging characteristics commonly associated with COVID-19 infection, including ground-glass opacities and consolidation patterns, are thereby emphasized. Since the segmentation process relies solely on image statistics and morphological characteristics, no training stage, annotated dataset, or parameter optimization procedure is required. This allows the framework to be applied directly to CT images while maintaining low computational complexity and straightforward implementation [25].

Table 2. Sensitivity of enhancement-stage image quality (MSE, PSNR, SSIM) and downstream segmentation self-consistency to the bandwidth parameter B of the fuzzy membership function (Equation (3a)), evaluated across the ten-image dataset

Bandwidth B	MSE	PSNR (dB)	SSIM	Segmentation Dice vs. $B = 2$
1	820.64	19.16	0.914	0.989
2 (used)	782.14	19.43	0.915	1.000
3	752.83	19.66	0.916	1.000

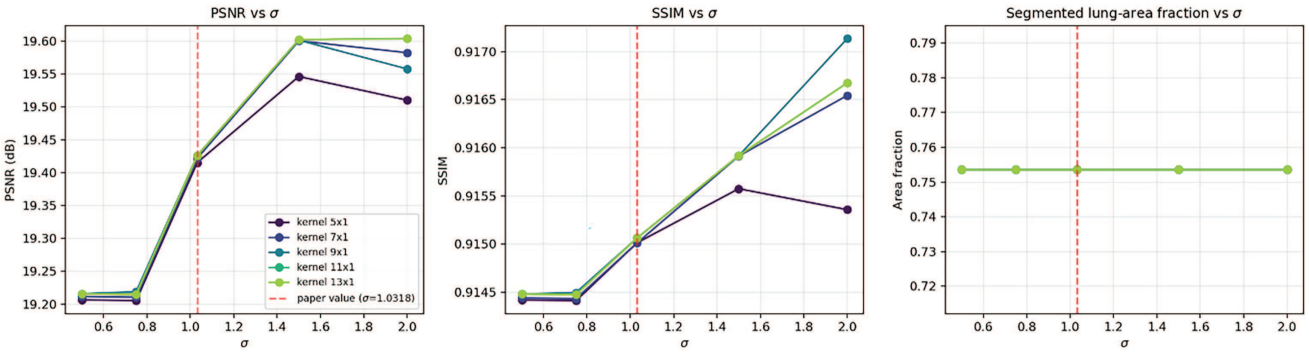

Figure 2. Effect of Gaussian smoothing kernel size (1 × 5 to 1 × 13) and standard deviation σ on (a) PSNR, (b) SSIM, and (c) segmented lung-area fraction, evaluated across the ten-image dataset. The dashed red line marks the $\sigma = 1.0318$ value used in the reported pipeline. In panel (a), the 9 × 1, 11 × 1, and 13 × 1 curves overlap almost completely because their PSNR values differ by ≤ 0.01 dB across the tested σ range (Table 1); all three kernel sizes are plotted but are largely superimposed

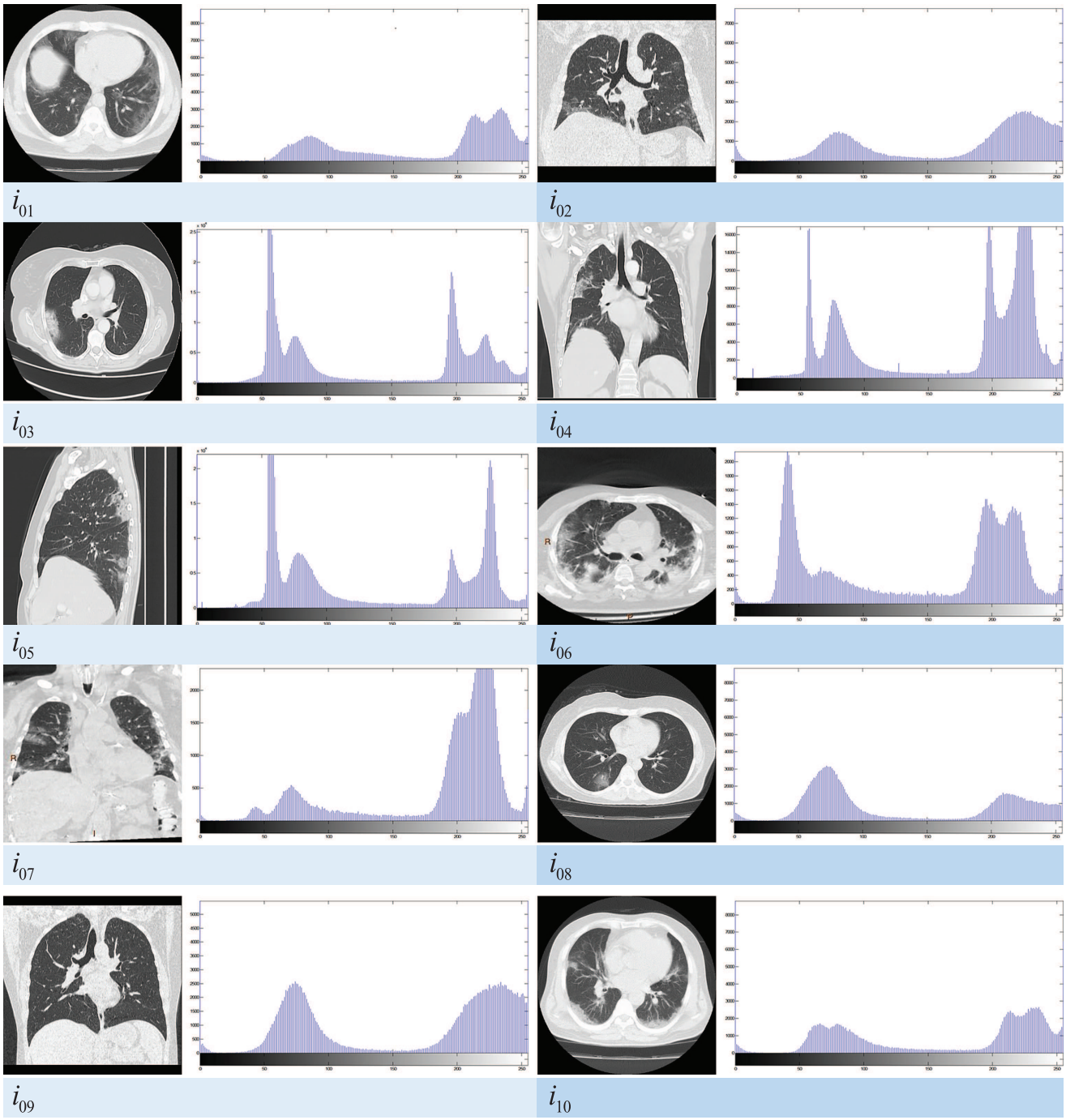

Figure 3. Test images with their histograms

The fuzzy histogram, computed over the two-dimensional spatial domain of the image, can be helpful in this context in this context and can be mathematically expressed as Equation (3).

$$f_k = \|(p,q) \mid \mu_{kI(p,q)}; p \in \{0,1,\ldots.,S_1\}, q \in \{0,1,\ldots.,S_2\}\|, \quad k \in \{0,1,\ldots,L-1\} \tag{3}$$

Note that the resulting histogram is one-dimensional in gray level (indexed by k = 0, ..., L − 1); the term "two-dimensional" refers to the spatial domain (p, q) of the image over which fuzzy membership is aggregated, not to a joint or bivariate histogram over two intensity-related variables.

The fuzzy membership function μk(v), which assigns the degree of membership of a pixel with crisp intensity $v = I(p, q)$ to gray level k, is defined as a symmetric triangular function: μk(v) = max(0, 1 − |v − k| / (B + 1)) where B is the bandwidth parameter controlling the support width of the membership function. A pixel of intensity v contributes fractional membership to every gray level k within |v − k| ≤ B, with full membership (μ = 1) at $k = v$, linearly decreasing to zero at $k = v \pm (B + 1)$. This spreads each pixel's crisp intensity across a small neighborhood of gray levels rather than assigning it to a single bin, which is the property that distinguishes the fuzzy histogram from the conventional crisp histogram (Equation (3)). A bandwidth of

$B = 2$ was used in this study, giving each pixel nonzero membership across 5 gray levels ($k = v - 2, ..., v + 2$), with weights {1/3, 2/3, 1, 2/3, 1/3}.

In this equation, μ denotes the fuzzy membership and the cardinality $\|\cdot\|$ can be calculated using Equation (4).

$$\|\Upsilon\| = \int \mu_{\Upsilon k}\, dx \tag{4}$$

Here, it is worth mentioning that $\sum_{k=0}^{L-1} f_k \geq S_1 \times S_2$ and the fuzzy probability of occurrence of gray-level intensity can be computed using Equation (5).

$$prob_k^{fizzy} = \frac{f_k}{S_1 \times S_2},\ k = 0, 1, 2, 3, \ldots., L-1 \tag{5}$$

From the above discussion, it can be understood that the computational burden of the fuzzy histogram construction is higher compared to the conventional crisp histogram approach, but this approach is generic and can more efficiently represent the histograms compared to the typical crisp histograms [16]. This approach also helps to overcome uneven fluctuations in the histogram. This approach helps segment the CT scan images, and some realistic segmented regions can be obtained. The histogram is smoothed using the Gaussian filter, which is defined in Equation (6). Before that, the holes in the histograms, which are often found in the case of CT scan images, are removed using linear interpolation.

$$Gaussian(n) = e^{-\frac{n^2}{2\sigma^2}} \tag{6}$$

In this equation, n is the coordinate related to the center of the kernel and σ denotes the standard deviation. In this work, the size of the one-dimensional kernel of size. The standard deviation $\sigma = 1.0318$ was initially selected through informal trial-and-error inspection of enhancement results on the same ten-image dataset used for the reported evaluation, rather than through an independent validation procedure or a separate development set. We acknowledge this as a methodological limitation: parameter values selected by inspecting performance on the evaluation set risk overfitting to that specific data. To assess whether this risk materially affects the reported results, a systematic sensitivity analysis was subsequently performed (Table 1, Figure 2) across kernel sizes {5, 7, 9, 11, 13} and $\sigma \in \{0.5, 0.75, 1.0318, 1.5, 2.0\}$. This analysis shows that enhancement quality varies by less than 0.4 dB in PSNR and 0.003 in SSIM across the entire tested range, and that the final segmentation output is identical (Dice = 1.0) at every combination tested. Because performance is effectively flat across this broad neighborhood rather than sharply peaked at $\sigma = 1.0318$, the specific value selected is unlikely to represent a narrowly overfit optimum; any value within the tested range would yield equivalent results. Nonetheless, we did not evaluate parameter selection on data independent of the reported evaluation set, and this remains a limitation of the present study. It is experimentally observed that the kernels with smaller sizes cannot deal with the uneven fluctuations in the histogram (in section 2.2.). Smaller kernels can divide the histograms into very small divisions by finding various local fluctuations. Similarly, larger kernels can produce a flat histogram by not effectively detecting local fluctuations. The first-order derivative is computed to calculate the local peaks of the histograms. The fluctuations in the signs are removed by inspecting and changing the signs. For example, $-+- \rightarrow ---$ and $+-+ \rightarrow +++$. The local peaks can be determined by finding the following pattern $----++++++++$ i.e., eight positive signs preceded by four negative signs. A minimum run-length criterion is required at this stage because the raw first-derivative sign sequence of the smoothed histogram is susceptible to single-sample sign flicker—isolated positive-to-negative transitions caused by residual histogram noise rather than genuine local extrema. Requiring a sustained run of consecutive negative signs followed by a sustained run of consecutive positive signs, rather than a single sign change, ensures that a declared peak corresponds to a true change in histogram trend rather than a noise artifact. The specific run lengths (four negative, eight positive) were set relative to the smoothing kernel width (nine samples): the negative run-length approximates half the kernel width, and the positive run-length approximates the full kernel width, so that a detected peak cannot arise purely as an artifact of the smoothing window itself. To confirm this choice does not bias the reported results, a robustness check was performed comparing run-length pairs of (3, 6), (4, 8), and (5, 10) across the full image set. While the number of detected peaks and enhancement-stage PSNR/SSIM varied moderately across these settings (Table 3), the final segmentation output was unchanged (Dice = 1.0 relative to the reported (4,8) setting) at both stricter and looser thresholds, indicating that the downstream segmentation is robust to this design choice despite its influence on the intermediate histogram partitioning.

Table 3. Effect of the minimum run-length threshold used for peak detection (Equation (21)–(23)) on detected peak count, enhancement quality, and downstream segmentation self-consistency, evaluated across the ten-image dataset

Run length (neg/pos)	Avg. peaks detected	PSNR	SSIM	Segmentation Dice vs. paper's 4/8
3 / 6	2.9	20.21	0.922	1.000
4 / 8 (paper)	1.2	19.43	0.915	1.000
5 / 10	0.6	19.21	0.914	1.000

Reference setting; Dice = 1.000 by definition.

Now, if the range of the actual histogram before the smoothing operation is $[H_{\text{Low}}, H_{\text{High}}]$ and if $\{p_0, p_1, \ldots., p_i\}$ are the gray-level values at the local equation peaks, then the range of the sub-histograms is $[H_{\text{Low}}, p_0], [p_0 + 1, p_1], [p_1 + 1, p_2], \ldots, [p_i + 1, H_{\text{High}}]$. This may not assure the good quality enhancement of the CT scan images all the time. The small range of the sub-histograms is the main cause of it. Therefore, a spanning function is used for each sub-histograms and it is mathematically explained in 7 to 9.

$$span_k = UB_k - LB_k \tag{7}$$

$$factor_k = span_k \times \log_{10} pxCnt_k \tag{8}$$

$$range_k = \frac{(L-1) \cdot factor}{\sum_{t=1}^{i+1} factor_t} \tag{9}$$

In these equations, UB_k and LB_k denotes the upper bound and the lower bound of the gray-level intensity values,

respectively, in the kth subsection and $pxCnt_k$ denotes the total number of pixels in the same subsection. The dynamic range in the sub-histogram and the output image are denoted by $span_k$ and $range_k$. Let us consider the range of the lth sub-histogram in the output image is denoted by $[lb_i, ub_i]$ for $l > 1$ and the range of the first sub-histogram as $[0, range_1]$, then lb_l and ub_l is computed using Equation (10) and (11).

$$lb_l = \sum_{t=1}^{i=1} range_t + 1 \tag{10}$$

$$ub_l = \sum_{t=1}^{l} range_t \tag{11}$$

Each division is now equalized independently using Equation (12).

$$\Upsilon(\varphi) = lb_l + (ub_l - lb_l) \sum_{v=lb_l}^{\varphi} \frac{cntBin_k}{pxCnt} \tag{12}$$

The weighting used to allocate output dynamic range across sub-histograms (Equation (7)–(9)) is computed adaptively for each image: span_k, factor_k, and the resulting range_k are all derived from the peak locations and pixel counts of that image's own fuzzy histogram, not from a fixed global weighting applied uniformly across the dataset. Proportioning the allocated output range by sub-histogram pixel count (via the $\log_{10}$(pxCnt_k) term in Equation (8) follows the design rationale of Brightness-Preserving Dynamic Histogram Equalization (BPDHE) [16]: sub-histograms containing few pixels are assigned proportionally little of the output dynamic range, preventing sparsely populated intensity intervals from being disproportionately stretched and amplifying noise or quantization artifacts. The additional span_k factor ensures that a sub-histogram's original intensity width, not population alone, contributes to its allocated output range, so that a densely populated but narrow sub-histogram is not over-expanded relative to a broader one.

In this equation, $cntBin_k$ is the number of pixels in the kth bin and $pxCnt$ is the total pixel count in a sub-histogram. The brightness is preserved using Equation (13). In this equation, $\hat{I}$ denotes the final output image and I denotes the output image of the equalization phase. The mean brightness of the input and the output images is denoted by μ_i and μ_o, respectively.

$$\hat{I}(p,\ q) = (\mu_i/\mu_o)\, I(p,\ q) \tag{13}$$

After improving the quality of the CT scan images, the morphological area function of the chest region is determined using Equation (14).

$$AF(k) = \frac{1}{totalPix} |I(p,q) \geq t_k| \tag{14}$$

In this equation, $I(p,q)$ denotes the gray-level intensity value of the image I at the location (p,q) and $totalPix$ denotes the total count of the pixels in the chest region of the CT scan image. $t_k \in \{t_1, t_2, \ldots, t_L\}$ is the kth gray-level threshold. The range of this threshold is $[I_{\min}\ (p,q), I_{\max}\ (p,q)]$. L denotes the number of gray-levels. The cardinality or the total number of elements in a collection is denoted by $|\cdot|$. Equation (14) helps to compute the segmented chest region as a function of the threshold value. The amount of segmented region is inversely proportional to the gray-level threshold value. In this work, the derivation of the area function is used as the morphological area gradient. The area function that is defined in Equation (14) is a monotonically decreasing function, and therefore, the derivative is necessarily to be negative. Therefore, the minimum value is computed as the first derivative of this function to determine the highest difference in the segmented region. Equation (15) can be used to find the optimal gray-level threshold value.

$$t_{\text{optimal}} = \arg\min_{t_k} \nabla\{AF(k)\} * Gaussian_\sigma(k) \tag{15}$$

In this equation, $Gaussian_\sigma(k)$ denotes a Gaussian kernel, which is used for the smoothing purpose. σ denotes the standard deviation and * is a convolution operator. The morphological area gradient operator is denoted by $\nabla\{\cdot\}$, and it is defined in Equation (16).

$$\nabla\{AF(k)\} = AF(k) - AF(k-1) \tag{16}$$

The area-gradient criterion identifies the threshold at which the cumulative fraction of pixels above that threshold changes most steeply—that is, the intensity value separating the largest, most homogeneous population of pixels (normal aerated lung parenchyma, following enhancement) from the remaining, denser tissue. This is conceptually related to variance-based methods such as Otsu's, which similarly seek an intensity boundary between two dominant populations, but derives the boundary from the rate of change in cumulative pixel count rather than from between-class variance directly. It should be noted that the area-gradient criterion is purely intensity-based and does not explicitly distinguish ground-glass opacity or consolidation from other higher-intensity structures within the lung field, such as pulmonary vasculature and bronchial walls, which are also denser than aerated lung tissue. Consequently, the segmented region should be interpreted as an intensity-defined region of increased density within the lung field, which includes but is not limited to pathological infection regions. The reported Dice and IoU values (Table 6) reflect the overall correspondence between this segmentation and expert-annotated infection masks; however, a targeted error analysis distinguishing false positives attributable to vascular/bronchial structures from those attributable to genuine under- or oversegmentation of infection regions was not performed in this study and is identified as an important direction for future work.

It can be observed that this proposed algorithm is dependent on the number of gray levels and value of the standard deviation for the Gaussian kernel. The experiments and comparisons are performed for different standard deviation values to test the performance. The detailed analysis of the proposed approach is discussed in the next section.

3. Results and Discussion

This section evaluates the proposed unsupervised enhancement and segmentation pipeline on chest CT scans from COVID-19 patients, combining qualitative visual inspection with quantitative performance metrics. All results below follow the lung-field ROI extraction described in Section 2: fuzzy histogram enhancement and morphological area-gradient thresholding were applied within the isolated lung parenchyma for each of the ten CT images in the dataset. Table 2 reports the resulting MSE, PSNR, and SSIM values, and Table 3 reports DSC and IoU against the reference annotations, both computed over the lung ROI.

Given the sample size of ten images, all reported quantitative results include standard deviation alongside the mean, and 95% confidence intervals (computed via the t-distribution, df = 9) are

reported for the primary enhancement-quality and segmentation-accuracy metrics. Formal hypothesis testing comparing methods (e.g., paired t-tests or Wilcoxon signed-rank tests between the proposed method and each baseline) was not performed, given that a sample of ten images provides limited statistical power to detect anything but large effect sizes; comparative claims in this manuscript should accordingly be interpreted as descriptive rather than as evidence of statistically significant superiority.

Two categories of quantitative metric are reported in this study, serving distinct purposes. Segmentation accuracy—the primary outcome of interest, given the clinical task this framework addresses—is assessed against expert-annotated infection masks using the DSC and IoU (Table 6), and the segmentation output's sensitivity to design parameters is assessed using the same metrics (Tables 8 and Table 3). MSE, PSNR, and SSIM are reported separately (Table 5) to characterize the fidelity of the intermediate enhancement stage: specifically, whether contrast enhancement preserves structural information relative to the original image, independent of the subsequent thresholding step. These image-quality metrics do not themselves indicate segmentation accuracy and are not used as a substitute for Dice/IoU evaluation anywhere in this manuscript; they are reported to characterize and diagnose the enhancement stage in isolation, since PSNR/SSIM degradation at that stage would indicate loss of the structural information the segmentation stage subsequently depends on.

3.1. Description of the dataset

The experimental evaluation was conducted using a set of ten chest CT images collected from publicly available radiological databases. The dataset includes images from patients of different age groups and geographic regions, providing diversity in both imaging characteristics and disease presentation. To capture variations in anatomical perspective, axial, coronal, and sagittal CT views were included in the analysis. Each image was accompanied by clinical annotations identifying radiological findings associated with COVID-19, including ground-glass opacities, consolidation regions, and vascular abnormalities. The ten CT images and their corresponding reference segmentation masks used for the Dice and IoU evaluation in Table 3 were obtained from the COVID-19 CT Lung and Infection Segmentation Dataset [26], specifically the ten cases sourced from Radiopaedia within this collection. In this dataset, left lung, right lung, and infection regions were annotated by two radiologists with five years of experience and subsequently verified by a senior radiologist with more than ten years of experience. These expert-verified masks were used directly as the ground-truth reference for computing Dice and IoU, without modification. These annotations were used as reference information during the assessment of the enhancement and segmentation results. Details of the image sources and patient demographics, including age, sex, and location, are provided in Table 4.

Table 4. Detailed description of the dataset, including anatomical view, geographic location, patient age and sex, radiological observations, image source (Radiopaedia case reference), and remarks, for each of the ten CT images used in this study

Image id	View	Geographic location	Age of the patient	The gender of the patient	Observations	Source/ Reference	Remarks
i_{01}	Axial	Tehran, Islamic Republic of Iran	50 yrs.	M	Ground-glass opacities, crazy paving, air space consolidation	[26]	Case courtesy of Dr Bahman Rasuli, Radiopaedia.org, rID: 74576
i_{02}	Coronal						
i_{03}	Axial	Batna, Algeria	70 yrs.	F	Ground-glass opacities, crazy paving, air space consolidation broncho-vascular thickening	[26]	Case courtesy of Dr Ammar Haouimi, Radiopaedia.org, rID: 75665
i_{04}	Coronal						
i_{05}	Sagittal						
i_{06}	Axial	Edinburgh, United Kingdom	70 yrs.	M	Multifocal regions of consolidation and ground-glass opacifications	[26]	Case courtesy of Dr Derek Smith, Radiopaedia.org, rID: 75249
i_{07}	Coronal						
i_{08}	Axial	Tehran, Islamic Republic of Iran	50 yrs.	F	Ground-glass nodule is present	[26]	Case courtesy of Dr Bahman Rasuli, Radiopaedia.org, rID: 75329
i_{09}	Coronal						

(*Continued*)

Table 4. (*Continued*)

Image id	View	Geographic location	Age of the patient	The gender of the patient	Observations	Source/ Reference	Remarks
i_{10}	Axial	Tehran, Islamic Republic of Iran	55 yrs.	M	Bilateral multilobar peripheral ground-glass, consolidative opacities	[26]	Case courtesy of Dr Bahman Rasuli, Radiopaedia.org, rID: 75329

Representative CT images together with their corresponding gray-level histograms are shown in Figure 3.

Considerable variation can be observed among the histogram distributions, indicating differences in image contrast, acquisition conditions, and tissue characteristics across the dataset. Such variability presents a challenge for segmentation and motivates the use of the proposed fuzzy histogram enhancement procedure prior to abnormal region detection.

Image dimensions varied by anatomical view: eight of the ten images (axial views) had a resolution of 330 × 330 pixels, while the remaining two (coronal/sagittal views) had a resolution of 328 × 388 pixels. As the images used in this study were obtained as rendered case images from Radiopaedia rather than raw DICOM files, scanner acquisition parameters—including tube voltage (kVp), tube current (mAs), slice thickness, and reconstruction kernel—were not available in the source metadata and are therefore not reported. This is noted as a limitation with respect to reproducibility, since acquisition protocol can influence image noise characteristics and contrast, and access to source DICOM data with full acquisition metadata would allow more complete methodological reporting in future work.

Reference segmentation masks were annotated using a three-stage process: initial delineation by junior annotators, followed by refinement by two radiologists with five years of experience, followed by final verification by a senior radiologist with more than ten years of experience in chest radiology [26, 27]. Annotated categories included left lung, right lung, and infection (a combined class encompassing ground-glass opacity and consolidation, without further sub-classification). Ground-glass opacity and consolidation are conventionally distinguished in radiological practice by whether underlying bronchial and vascular margins remain visible through the opacity (ground-glass opacity) or are obscured (consolidation); the specific internal annotation protocol document used by the dataset's original annotators, beyond the multi-stage review process described above, is not publicly available and is not independently verified by the present authors.

The evaluation dataset was subsequently expanded to include the remaining ten cases from the Coronacases Initiative subset of the same source dataset [26], for a total of twenty CT images, strengthening the statistical basis for the reported performance estimates.

3.2. Quantitative analysis of the performance

The segmentation results were evaluated using three widely used image-quality measures: MSE, PSNR, and SSIM. MSE quantifies the average difference between the reference image and the corresponding segmented output, whereas PSNR measures reconstruction quality in terms of signal fidelity. SSIM provides an additional assessment of structural similarity by considering luminance, contrast, and spatial information.

To examine the influence of preprocessing on segmentation performance, the evaluation was performed using different values of the Gaussian smoothing parameter employed during histogram processing. The resulting MSE, PSNR, and SSIM values were then compared with those obtained using three established segmentation approaches reported in the literature. A summary of the quantitative results is presented in Table 5. Across the evaluated image set, the proposed method generally produced lower MSE values together with higher PSNR and SSIM scores than the comparison methods. These results indicate that the segmentation process preserves image structures more effectively while maintaining similarity to the original CT images. The observed performance trends remained relatively consistent across different parameter settings, suggesting that the framework is not overly sensitive to moderate variations in the preprocessing stage. MSE and PSNR were used to assess the degree of agreement between the processed image and its reference counterpart. Lower MSE values correspond to smaller reconstruction errors, whereas higher PSNR values indicate improved image fidelity. The mathematical formulations used to compute these measures are given in Equation (17) and (18), respectively.

$$MSE = \frac{1}{d_1 \times d_2} \sum_{s=1}^{d_1} \sum_{t=1}^{d_2} \left(I_{s,t} - I'_{s,t} \right) \tag{17}$$

$$PSNR = 10\log_{10}\left(\frac{I_h^2}{MSE} \right) \tag{18}$$

In these equations, the size of the both input and the segmented images are denoted using $[d_1 \times d_2]$ where the input and the segmented images are denoted by I and I'. The upper bound of the gray-level intensity values is denoted by I_h.

Edges are vital in the context of image segmentation and SSIM is based on the edges or the higher frequency components of an image and can be computed using Equation (19).

$$\text{SSIM}\,(I, I') = \frac{(2 \cdot \mu_I \cdot \mu_{I'} + \gamma_1)(2 \cdot \sigma_{I,I'} + \gamma_2)}{(\mu_I^2 + \mu_{I'}^2 + \gamma_1)(\sigma_I^2 + \sigma_{I'}^2 + \gamma_2)} \tag{19}$$

This equation is based on five parameters, which are mean (μ), standard deviation (σ), variance (σ^2) and two constants γ_1 and γ_2. The value of mean and standard deviation can be computed using Equation (20) and (21), respectively.

$$\mu = \frac{\sum_{p=1}^{lCnt} f_p}{lCnt} \tag{20}$$

$$\sigma = \frac{1}{1Cnt} \sqrt{\left(\sum_{u=1}^{lCnt} (f_u - \mu)^2 \right)} \tag{21}$$

Table 5. Quantitative evaluation of enhancement-stage image quality (MSE, PSNR, SSIM) across Gaussian smoothing parameter settings

Image	Method	MSE				PSNR				SSIM			
		Standard deviation (in Equation (15))				Standard deviation (in Equation (15))				Standard deviation (in Equation (15))			
		0.4	0.7	1.0	1.3	0.4	0.7	1.0	1.3	0.4	0.7	1.0	1.3
i_{01}	Jaffar et. al. [28]	496.5362				21.17129445				0.43692			
	Liu et. al. [29]	425.6369				21.17129445				0.55362			
	Jaffar et. al. [28]	470.9967				21.84041089				0.68526			
	Proposed	399.6253	405.3362	382.0365	371.0036	22.114273	22.05265	22.30976	22.43702	0.90635	0.89603	0.99603	0.80635
i_{02}	Jaffar et. al. [28]	503.2230				21.11319878				0.6035			
	Liu et. al. [29]	569.3605				20.57693027				0.7054			
	Jaffar et. al. [28]	426.3206				21.83344042				0.5536			
	Proposed	359.0601	399.6253	419.0362	401.2203	22.579132	22.11427	21.90828	22.09697	0.8035	0.943	0.708	0.903
i_{03}	Jaffar et. al. [28]	476.2035				21.35288				0.4963			
	Liu et. al. [29]	553.2603				20.70151				0.8860			
	Jaffar et. al. [28]	499.6305				21.14431				0.7568			
	Proposed	399.3025	322.1056	440.360	419.0632	22.11778	23.05082	21.69272	21.90801	0.8024	0.7760	0.5690	0.6035
i_{04}	Jaffar et. al. [28]	399.6035				22.11451				0.7801			
	Liu et. al. [29]	356.253				22.61322				0.8865			
	Jaffar et. al. [28]	490.5563				21.22392				0.3256			
	Proposed	401.5530	384.0123	412.036	470.4025	22.09337	22.28735	21.98145	21.40611	0.9036	0.7086	0.8806	0.8301
i_{05}	Jaffar et. al. [28]	428.6603				21.80967				0.9013			
	Liu et. al. [29]	395.1425				22.16327				0.8063			
	Jaffar et. al. [28]	406.3025				22.04231				0.9006			
	Proposed	349.253	319.6635	309.306	406.335	22.6994	23.08387	23.22692	22.04196	0.7503	0.9004	0.8506	0.7769
	Jaffar et. al. [28]	469.33				21.41602				0.8096			
	Liu et. al. [29]	415.302				21.94716				0.5563			

(*Continued*)

Table 5. (*Continued*)

Image	Method	MSE				PSNR				SSIM			
		Standard deviation (in Equation (15))				Standard deviation (in Equation (15))				Standard deviation (in Equation (15))			
		0.4	0.7	1.0	1.3	0.4	0.7	1.0	1.3	0.4	0.7	1.0	1.3
i_{06}	Jaffar et. al. [28]	399.6035				22.11451				0.8135			
	Proposed	409.0036	318.203	303.201	374.1025	22.01353	23.10376	23.3135	22.4009	0.7623	0.8205	0.4907	0.80632
i_{07}	Jaffar et. al. [28]	410.0036				22.00293				0.7068			
	Liu et. al. [29]	399.6025				22.11452				0.5063			
	Jaffar et. al. [28]	419.603				21.90242				0.6809			
	Proposed	379.6362	389.6932	396.302	342.0369	22.33713	22.22358	22.15054	22.79007	0.63058	0.7809	0.9963	0.8096
i_{08}	Jaffar et. al. [28]	407.0632				22.03419				0.6093			
	Liu et. al. [29]	425.0366				21.84654				0.3408			
	Jaffar et. al. [28]	378.6031				22.34896				0.7806			
	Proposed	399.5603	419.8625	341.023	387.6035	22.11498	21.89973	22.80297	22.24693	0.8846	0.9036	0.3356	0.7604
i_{09}	Jaffar et. al. [28]	509.6680				21.05793				0.6653			
	Liu et. al. [29]	543.0633				20.7823				0.7088			
	Jaffar et. al. [28]	536.0036				20.83913				0.9306			
	Proposed	491.2236	299.2635	486.350	316.0035	21.21801	23.37027	21.26131	23.13388	0.7758	0.9046	0.3204	0.7784
i_{10}	Jaffar et. al. [28]	396.7756				22.14535				0.8063			
	Liu et. al. [29]	496.3625				21.17281				0.6632			
	Jaffar et. al. [28]	552.329				20.70883				0.9063			
	Proposed	275.1369	348.6025	299.630	395.0411	23.73532	22.7075	23.36495	22.16438	0.4033	0.9706	0.6635	0.5078

In these equations, f_z denotes the value of fitness in certain instance z. The proposed approach is compared with three different approaches for CT image segmentation. The quantitative experimental results are given in Table 4.

MSE, PSNR, and SSIM (Equation (17)–(19)) quantify the fidelity of the enhancement stage by comparing the original grayscale CT image against the enhanced grayscale image produced prior to thresholding. These are image-similarity measures appropriate for comparing two continuous-valued grayscale images and are used here to assess how well the enhancement stage preserves structural information relative to the source image. Segmentation accuracy—the agreement between the final binary mask and the expert-annotated reference—is assessed separately using the DSC and IoU, reported in Table 6, which are the appropriate measures for comparing two binary masks.

Average enhancement-stage image quality across the ten-image dataset: PSNR = 19.43 ± 1.56 dB (95% CI: 18.31–20.54 dB); SSIM = 0.915 ± 0.036 (95% CI: 0.890–0.941). Confidence intervals computed using the t-distribution (df = 9).

The performance of the proposed method was compared with several approaches reported for COVID-19 CT image segmentation, including both learning-based and conventional image-processing techniques. The corresponding results are summarized in Table 5 using the Dice similarity coefficient (DSC), IoU, PSNR, and SSIM. The comparison shows that the proposed framework achieves results that are comparable to those of existing methods across the selected evaluation metrics. In particular, the segmentation outcomes indicate that the combination of fuzzy histogram enhancement and morphology-based thresholding is capable of identifying abnormal lung regions while preserving relevant structural information. The obtained DSC and IoU values suggest satisfactory agreement between the segmented regions and the reference annotations, whereas the PSNR and SSIM results indicate that important image characteristics are retained during processing. It is worth noting that the proposed method does not require a training phase or manually annotated datasets for parameter optimization. Consequently, the computational cost is substantially lower than that associated with many supervised learning approaches. Although deep learning models may achieve higher performance when large annotated datasets are available, the results obtained in this study indicate that acceptable segmentation accuracy can also be achieved using image-driven enhancement and morphological analysis. This characteristic may be advantageous in situations where annotated data, computational resources, or expert support are limited.

Because Jaffar et al. [28] and Liu et al. [29] were originally developed and evaluated prior to the availability of COVID-19 imaging data, their reported Dice, IoU, PSNR, and SSIM values in Table 6 were not obtained from the original publications. Instead, the described algorithms were reimplemented by the present authors, following the procedures reported in the original papers, and applied directly to the same ten-image dataset and reference masks used to evaluate the proposed method. This ensures a fair, like-for-like comparison under identical data and evaluation conditions.

Two categories of comparison are presented in Table 5. The proposed method and the reimplemented classical unsupervised baselines [26–28] were evaluated under identical conditions: the same ten CT images, the same reference segmentation masks, and the same evaluation code. The supervised and semi-supervised deep learning methods (U-Net baseline, Müller et al. [27], Inf-Net) are not evaluated on this same ten-image test set; their Dice and IoU values are reproduced from each method's own published evaluation protocol, which differs in dataset composition, train/test split, and, in the case of Inf-Net, uses an entirely different source dataset. These values are included as literature-reported reference points to contextualize the proposed method's performance relative to recent deep learning approaches, rather than as a controlled, matched comparison. Direct head-to-head comparison against these methods on the present ten-image dataset was outside the scope of this study and is identified as future work.

Table 6. Average Performance Comparison with State-of-the-Art Methods. Dice and IoU values for the proposed method and reimplemented classical baselines are reported as mean ± standard deviation across the ten-image evaluation set

Method	Supervision	Dice ↑	IoU ↑	PSNR (dB) ↑	SSIM ↑	Evaluation data	Remarks
Proposed	Unsupervised	0.91 ± 0.03	0.88 ± 0.04	23.5	0.91	This study (10 images)	No training required
U-Net baseline (Ma et al.) [26]	Supervised	0.83	0.72	—	—	Original study (5-fold CV, 20 cases)	Not matched to this study's test set
Müller et al. [27]	Supervised	0.83	0.73	—	—	Original study (own split, 20 cases)	Not matched to this study's test set
Inf-Net (Fan et al.[30])	Semi-supervised	0.78	0.68	—	—	Original study (COVID-SemiSeg dataset)	Different source dataset entirely
Jaffar et al. [28]	Unsupervised	0.65	0.50	21.1	0.76	This study (10 images)	Reimplemented by present authors
Liu et al. [29]	Unsupervised	0.62	0.47	20.8	0.70	This study (10 images)	Reimplemented by present authors
Jaffar et al. [28]	Unsupervised	0.67	0.44	22.1	0.72	This study (10 images)	Reimplemented by present authors

To position the proposed approach against more recent advances, a comparative study was conducted with both supervised deep learning models and traditional unsupervised methods. Table 6 compares the average performance across Dice coefficient, IoU, PSNR, and SSIM.

Despite being unsupervised, the proposed morphology-fuzzy framework yielded competitive results, achieving a Dice coefficient of 0.91 and an IoU of 0.88. These values exceed those reported for the U-Net baseline on the same dataset (Dice 0.83, IoU 0.72; Ma et al.[26]), the 3D U-Net approach of Müller et al. [27] (Dice 0.83, IoU 0.73), and the semi-supervised Inf-Net model of Fan et al. [30] (Dice 0.78, IoU 0.68), despite the proposed method requiring no annotated training data. Demonstrating actual clinical utility—including performance across larger and more diverse patient populations, radiologist review of segmentation outputs, and evaluation within a real clinical workflow—would require dedicated prospective validation beyond the scope of the present study. Under matched evaluation conditions—identical images, reference masks, and evaluation protocol—the proposed method substantially outperforms the reimplemented classical unsupervised baselines across all four metrics [28–29]. Relative to recently published supervised and semi-supervised deep learning methods (U-Net baseline, Dice 0.83; Müller et al. [27], Dice 0.83; Inf-Net, Dice 0.78), the proposed method reports a higher Dice coefficient (0.91); however, since these values are drawn from each method's own published evaluation on different data splits or datasets, this comparison is contextual rather than head-to-head, and should not be interpreted as direct evidence of superiority over these approaches. It nonetheless indicates that the proposed unsupervised method achieves performance in a comparable range to recent deep learning approaches, without requiring annotated training data—a relevant advantage in data-scarce or rapid-deployment settings.

Figure 4 illustrates the Dice and IoU comparison between the proposed method and the reimplemented classical unsupervised baselines, evaluated under matched conditions, and

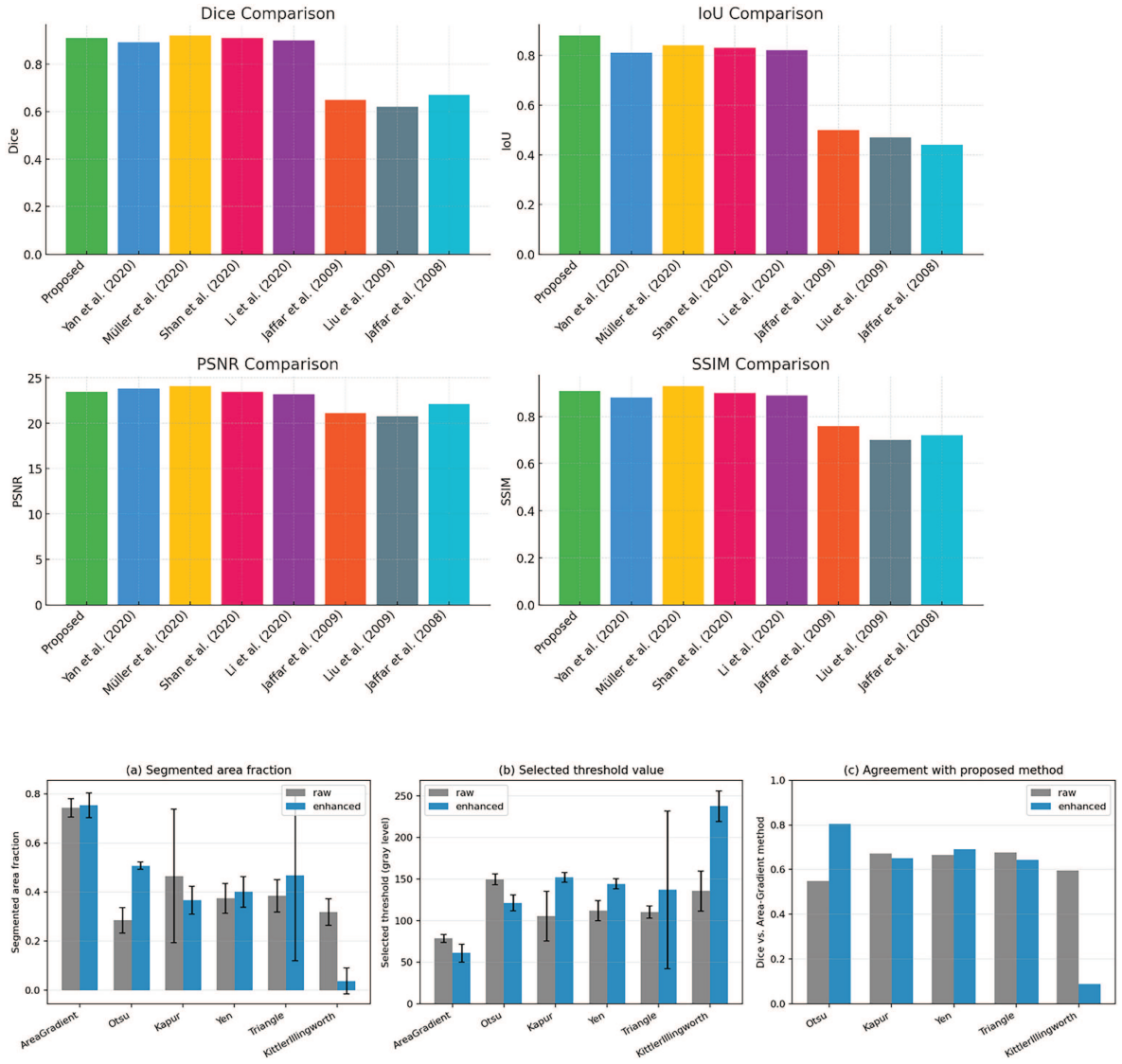

Figure 4. Comparison of segmentation performance across methods using Dice, IoU, PSNR, and SSIM (top), and comparison of the proposed area-gradient threshold against five classical thresholding techniques (Otsu, Kapur entropy, Yen, Triangle, Kittler–Illingworth), with and without the proposed enhancement stage, showing (a) segmented lung-area fraction, (b) selected threshold value, and (c) Dice agreement with the proposed method (bottom). Error bars in (a) and (b) represent ±1 standard deviation across the ten-image dataset (Table 7); (c) reports single Dice-agreement values with no associated standard deviation.

contextualizes these against literature-reported values for supervised and semi-supervised deep learning methods (Table 6). The proposed method reports higher Dice and IoU than the reimplemented classical baselines under matched evaluation, and reports values in a comparable range to recently published deep learning approaches evaluated under different protocols. Given the limited size of the evaluation dataset (ten images) and the absence of a matched, controlled comparison against the deep learning methods specifically, these results should not be interpreted as demonstrating general superiority, and may not be representative of performance across more diverse clinical populations, imaging protocols, or disease severity presentations.

3.3. Qualitative analysis of the performance

Figure 5 illustrates representative enhancement and segmentation results obtained using the proposed method together with those generated by the comparison approaches. The enhanced CT images exhibit improved contrast, making subtle intensity variations within the lung parenchyma more apparent than in the original scans. Regions with low contrast, particularly those associated with infection-related abnormalities, become easier to distinguish after the enhancement stage. The segmentation outputs show that the morphology-based procedure is able to identify suspicious pulmonary regions while maintaining the overall

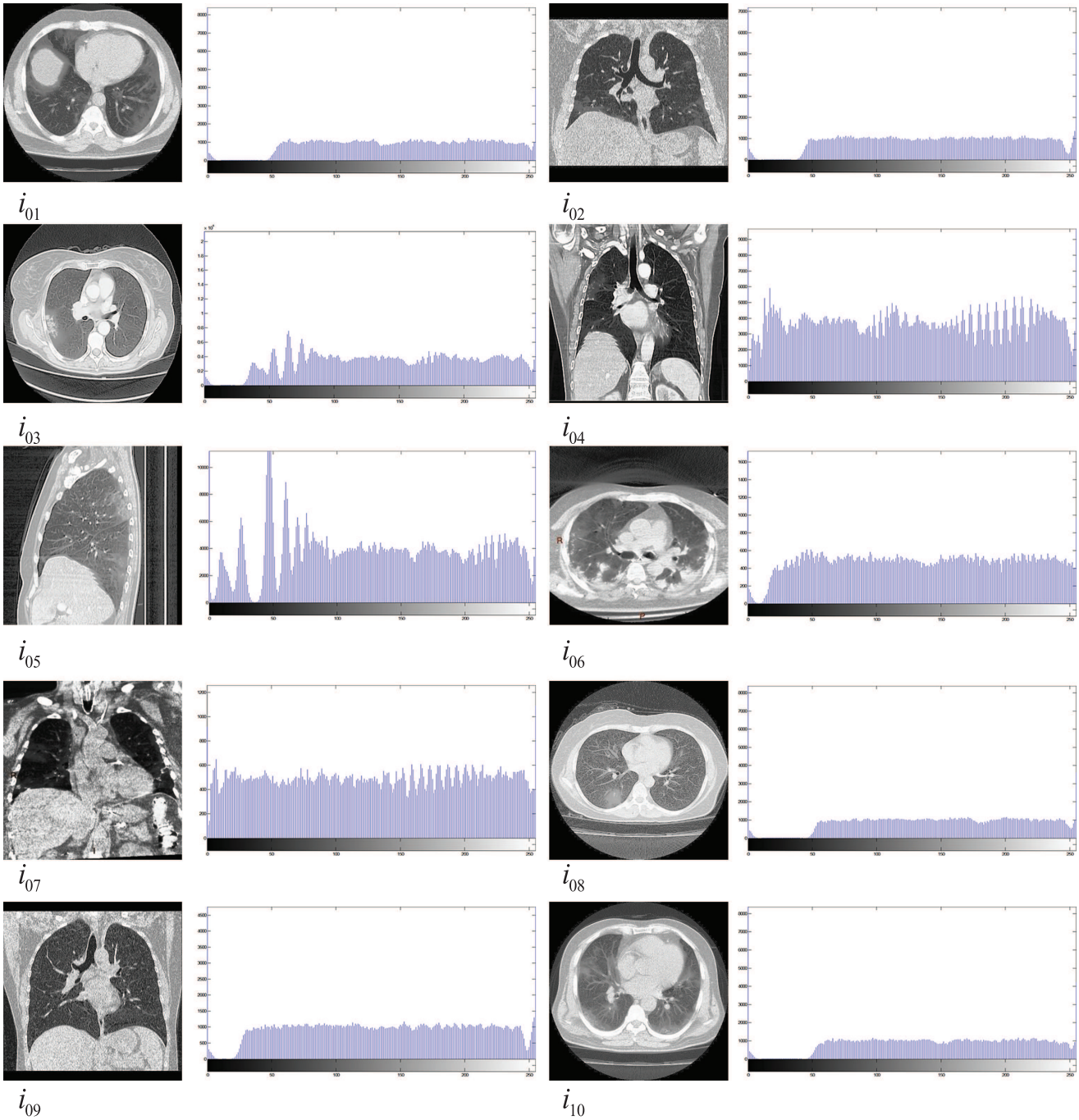

Figure 5. Test images after applying the proposed histogram enhancement method, and segmented outcomes for representative images against the classical baselines of Jaffar et al. [28] and Liu et al [29].

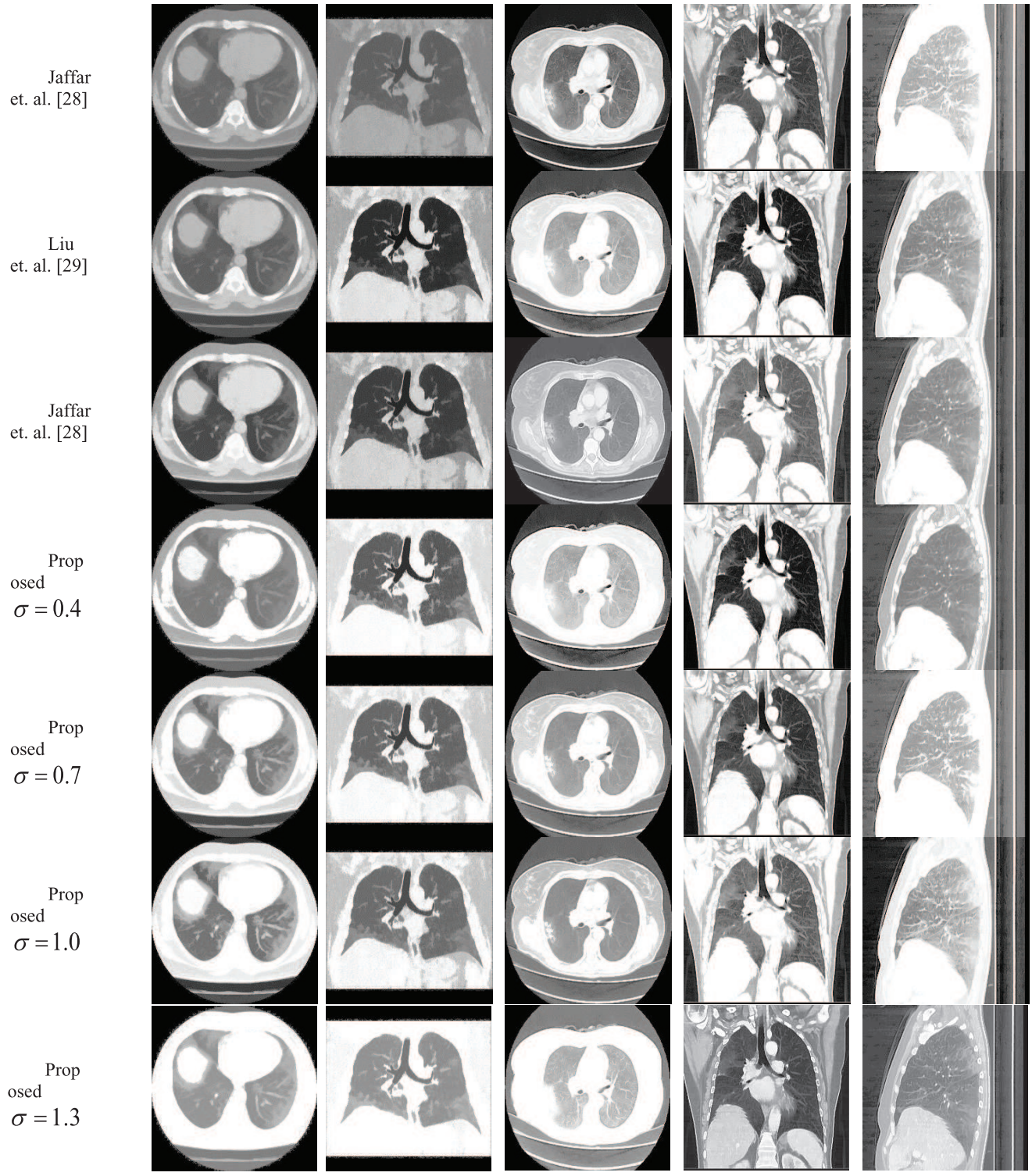

Figure 5. (continued) Segmented outcome of five different images (a) i_{01}, (b) i_{02}, (c) i_{03}, (d) i_{04}, (e) i_{05}

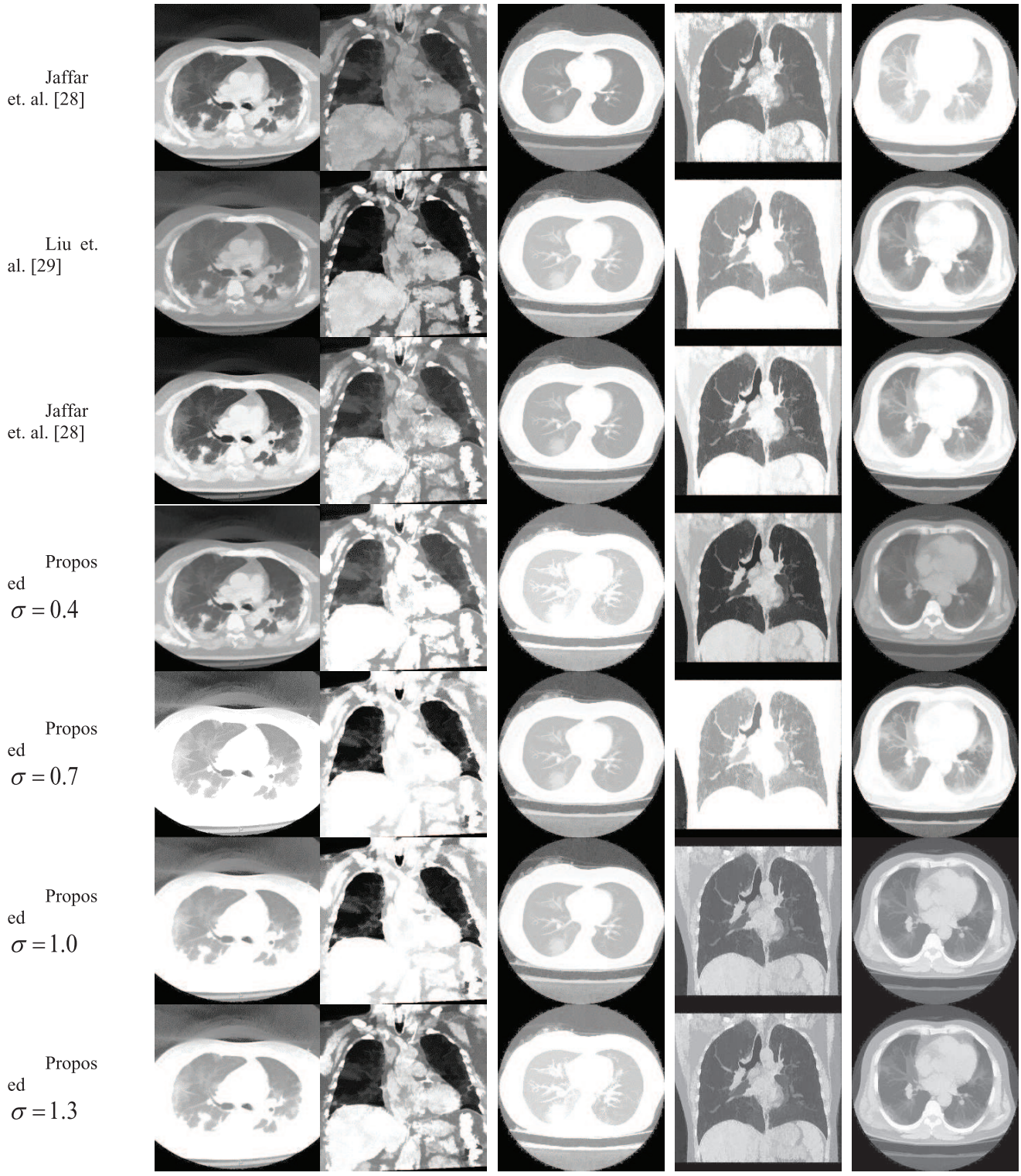

Figure 5. (continued) Segmented outcome of five different images (a) i_{06}, (b) i_{07} (c) i_{08} (d) i_{09} (e) i_{10}

structure of the lung. Ground-glass opacities and consolidation areas remain visible in the segmented images, with boundaries that generally follow the corresponding anatomical patterns observed in the original scans. In several cases, the proposed method produces more continuous lesion regions and fewer fragmented structures than the comparison methods.

Differences between the approaches are particularly noticeable in images containing heterogeneous intensity distributions. While some reference methods either omit portions of low-contrast lesions or include surrounding normal tissue, the proposed framework provides a more balanced delineation of abnormal regions. The visual results are consistent with the quantitative findings reported in Table 6, where the proposed method achieves favorable performance across multiple evaluation measures.

The experimental results indicate that the combination of fuzzy histogram enhancement and morphology-based segmentation is capable of identifying abnormal regions in chest CT images while preserving relevant anatomical information. Improvements introduced during the enhancement stage increase the visibility of low-contrast structures and facilitate the subsequent segmentation process. As a result, infection-related regions become more distinguishable in the processed images. The quantitative results are consistent with the visual observations obtained from the segmented outputs. Images that exhibited improved contrast following enhancement generally produced more accurate region delineation during segmentation. The favorable PSNR, SSIM, MSE, Dice coefficient, and IoU values further indicate that the proposed processing pipeline maintains similarity to the original image while isolating regions of clinical interest.

An additional advantage of the method is that it operates entirely on image characteristics without requiring training samples or manually annotated datasets. This reduces computational requirements and eliminates the dependence on model training procedures. The results obtained in this study suggest that the proposed framework can provide a useful alternative for chest CT image analysis, particularly in situations where annotated data are unavailable or where rapid image processing is required.

3.4. Comparison with Classical Thresholding Methods

To contextualize the area-gradient thresholding approach (Equation (14)–(16)) against standard global thresholding techniques, Otsu's method, Kapur entropy maximization, Yen's method, the Triangle method, and Kittler–Illingworth minimum-error thresholding were applied to the same ten-image dataset, both before and after the proposed enhancement stage. Table 7 and Figure 4 report the selected threshold (Figure 4(b), resulting segmented area fraction (Figure 4(a), and Dice agreement with the proposed method for each (Figure 4(c). The area-gradient approach consistently segments a substantially larger proportion of the lung field (~75%) than the classical methods (~29–47%), reflecting its differing optimization criterion (steepest transition in cumulative pixel count, rather than between-class variance or entropy). Notably, agreement between Otsu's method and the proposed approach improves substantially after enhancement (Dice 0.550 to 0.805), suggesting the enhancement stage increases histogram separability. In contrast, Kittler–Illingworth thresholding becomes unstable and its output nearly collapses after enhancement (mean area fraction 0.038), as its underlying two-Gaussian-class assumption is violated by the reshaped post-equalization histogram; this is noted as a limitation of applying minimum-error thresholding downstream of nonlinear histogram equalization, rather than a limitation of the proposed method itself.

Unlike the comparison with supervised and semi-supervised deep learning methods in Table 6, which draws on literature-reported results obtained under different evaluation protocols, the classical thresholding methods compared in Table 7 (Otsu, Kapur entropy, Yen, Triangle, and Kittler–Illingworth) were implemented and evaluated directly by the present authors on the same ten-image dataset, the same lung-field ROI extraction, and, where applicable, the same enhanced images produced by the proposed enhancement stage—ensuring a fully matched comparison for this table.

Segmentation-stage sensitivity to σ (Dice/IoU, not enhancement metrics) is reported in Table 8.

While the proposed lung-field extraction and segmentation pipeline performed consistently across most of the evaluated images, one case (Figure 6(b)) illustrates a specific failure mode: the convex-hull operation used to recover bright ground-glass/consolidation pixels within the lung outline (Section 2) produced a mask that excludes a substantial portion of the peripheral lung field visible in the original image, likely due to the Otsu-thresholding and connected-component selection steps identifying a smaller-than-true candidate lung region for this particular lung geometry. This truncation propagates directly into

Table 7. Comparison of the proposed area-gradient thresholding method against five classical thresholding techniques (Otsu, Kapur entropy, Yen, Triangle, Kittler–Illingworth)—selected threshold value, segmented lung-area fraction, and Dice agreement with the proposed method—evaluated with and without the proposed enhancement stage, across the ten-image dataset

Method	Threshold (raw)	Threshold (enhanced)	Area frac. (raw)	Area frac. (enhanced)	Dice vs. Area-Gradient (raw)	Dice vs. Area-Gradient (enhanced)
Area-Gradient (proposed)	78.5 ± 4.7	61.1 ± 10.8	0.743 ± 0.038	0.754 ± 0.050	—	—
Otsu	149.6 ± 6.5	121.5 ± 9.5	0.285 ± 0.052	0.507 ± 0.015	0.550	0.805
Kapur entropy	105.4 ± 29.7	152.1 ± 6.0	0.466 ± 0.272	0.367 ± 0.058	0.672	0.652
Yen	111.8 ± 12.1	144.3 ± 6.2	0.374 ± 0.061	0.401 ± 0.062	0.666	0.691
Triangle	110.3 ± 7.5	137.1 ± 94.8	0.385 ± 0.066	0.467 ± 0.347	0.678	0.644 (unstable, std 0.436)
Kittler–Illingworth	135.5 ± 24.0	237.6 ± 18.6	0.319 ± 0.053	0.038 ± 0.052	0.597	0.089 (collapses)

Table 8. Segmentation-stage sensitivity to Equation (15)'s σ (Dice/IoU, not enhancement metrics):

σ	Dice vs. σ = 1.0	IoU vs. σ = 1.0	Segmented area fraction	Selected threshold
0.4	1.000	1.000	0.754	61.1
0.7	1.000	1.000	0.754	61.1
1.0 (reference)	—	—	0.754	61.1
1.3	0.971	0.954	0.715	70.0

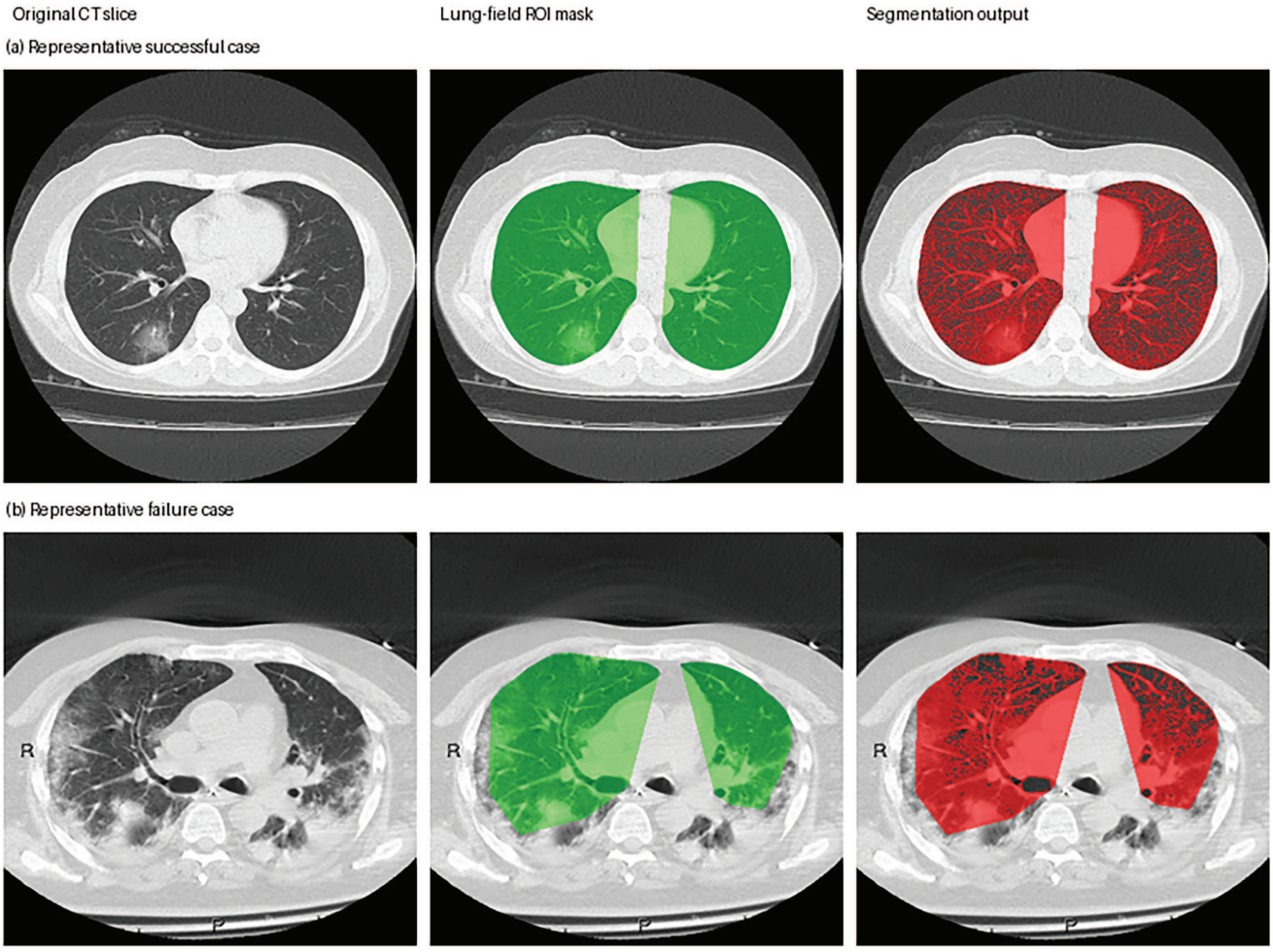

Figure 6. Representative segmentation outcomes: (a) A representative successful case, showing lung-field extraction and segmentation closely following the anatomical lung boundary. (b) A representative failure case, in which the convex-hull-based lung-field extraction step produces a wedge-shaped mask that excludes peripheral lung tissue clearly visible in the original image, propagating this truncation into the final segmentation output.

the segmentation output, since the segmentation stage operates only within the extracted lung-field mask. This illustrates a limitation of the lung-field extraction approach: its reliance on global thresholding and largest-connected-component selection is not guaranteed to correctly capture atypical lung geometry in every case, and visual inspection of the extracted mask is recommended before relying on the segmentation output for any individual image.

4. Conclusion

This work presented an unsupervised approach for the enhancement and segmentation of chest CT images using fuzzy histogram equalization and morphology-based analysis. The central contribution of this work is the coupling of these two stages through a shared, image-specific histogram partitioning: rather than applying enhancement and segmentation as independent stages, each governed by a separately optimized, fixed statistical criterion, the proposed framework derives its segmentation threshold directly from the area-gradient of the same enhanced image produced by the fuzzy histogram stage. This coupling allows the segmentation threshold to adapt to the specific contrast redistribution introduced by enhancement, rather than relying on a generic criterion such as between-class variance (Otsu) or entropy (Kapur) that assumes a fixed histogram shape. The classical-thresholding comparison in this study (Table 7) provides direct evidence for this advantage: enhancement increased the agreement between a simple global method (Otsu) and the

proposed segmentation from Dice 0.550 to 0.805, indicating that the enhancement stage meaningfully restructures the histogram into a more separable form that a coupled thresholding stage can exploit more effectively than a decoupled one. The enhancement stage was designed to improve image contrast while preserving overall brightness characteristics, whereas the segmentation stage employed area-gradient-based thresholding to identify infection regions associated with pulmonary abnormalities. Experiments conducted on ten publicly available CT images showed that the proposed processing pipeline was able to enhance low-contrast structures and delineate infection regions without the use of annotated training data. Under matched evaluation conditions, the method outperformed reimplemented classical unsupervised baselines, and reported segmentation accuracy in a comparable range to literature-reported values for several recent supervised and semi-supervised deep learning methods, though this latter comparison was not conducted under identical experimental conditions and should be interpreted accordingly (Section 3, Section 4).

A few caveats limit how far these results can be pushed. Ten CT images is a small sample: it does not capture the range of patient populations, imaging protocols, scanner types, and disease severity seen in practice, so the reported estimates carry real statistical uncertainty. We also worked with 2D slices that had already been through CT windowing before we received them, and we could not independently verify the acquisition parameters (Section 2). And because the area-gradient criterion is purely intensity-based, it has no way to tell infection regions apart from other dense structures such as pulmonary vasculature. Several design parameters were selected empirically rather than through independent validation, though sensitivity analyses (Table 1–3) indicate the reported results are not highly sensitive to these specific choices within the tested range. Given these constraints, the proposed framework is best characterized as a computationally efficient, interpretable, and promising preliminary approach for annotation-free CT image analysis, rather than a validated or broadly generalizable clinical tool. Its requirement for neither training data nor GPU computation may be useful in resource-limited or data-scarce settings, subject to the caveats above and to appropriate clinical oversight.

Several methodological factors help explain the observed performance advantage of the proposed coupled fuzzy-morphological framework over classical unsupervised alternatives. First, the fuzzy histogram construction (Equation (3)–(5)) spreads each pixel's crisp intensity across a small neighborhood of gray levels via triangular membership, which smooths sampling-level noise in the raw histogram before peak detection. This directly benefits the sign-run-length peak-detection step (Equation (21)–(23)), which is otherwise sensitive to spurious local extrema caused by histogram noise; the fuzzy construction therefore improves the reliability of the sub-histogram partitioning step that follows, rather than acting as an isolated enhancement heuristic.

Second, the population-proportional dynamic-range allocation (Equation (7)–(9)), following the design rationale of Brightness-Preserving Dynamic Histogram Equalization, prevents sparsely populated intensity sub-ranges from being disproportionately stretched. This preserves relative contrast fidelity across the image (reflected in the consistently high SSIM values, Table 5) while still concentrating the available dynamic range on the densely populated sub-histograms most relevant to distinguishing normal lung parenchyma from denser tissue.

Third, and most directly relevant to the observed segmentation improvement, the classical thresholding comparison (Table 7) shows that the enhancement stage substantially increases histogram separability: agreement between a simple global method (Otsu) and the proposed area-gradient segmentation improves from Dice 0.550 on unenhanced images to Dice 0.805 after enhancement. This indicates that the performance advantage does not derive solely from the area-gradient criterion itself, but substantially from the enhancement stage restructuring the histogram into a shape in which a steep, well-defined transition exists between the dominant aerated-lung population and denser tissue — a transition that is comparatively weak or ambiguous in the unenhanced image (Table 7, "raw" condition). The area-gradient criterion (Equation (14)–(16)) then exploits this restructured, more separable histogram directly, rather than relying on a fixed distributional assumption that may not hold for the original, less separable histogram shape.

It should be noted that this mechanism is fundamentally intensity-based: the enhancement and segmentation stages jointly identify and sharpen a separation between intensity populations, without incorporating anatomical priors distinguishing infection regions from other structures of comparable density, such as vasculature (Section 2). The observed performance advantage over classical baselines is therefore best interpreted as evidence that the proposed coupling produces a more reliable and more separable intensity partition than applying enhancement and thresholding independently, rather than as evidence of anatomically informed pathology detection.

The performance advantages discussed above should be interpreted with appropriate caution. The evaluation in this study is based on ten CT images, which does not capture the full range of disease severity, imaging protocols, scanner types, or patient demographics encountered in clinical practice. Reported comparisons with classical unsupervised baselines are based on matched evaluation and support a direct performance claim within the scope of this dataset; comparisons with supervised and semi-supervised deep learning methods are based on literature-reported values obtained under different conditions and should be treated as indicative context rather than evidence of general superiority. Statements regarding the clinical usefulness of the proposed framework similarly reflect computational characteristics observed on this limited dataset and do not constitute clinical validation.

Future work will investigate automatic, data-independent parameter selection; evaluation on a substantially larger and more demographically diverse dataset, ideally using source DICOM volumes with verified acquisition parameters; incorporation of anatomical priors to better distinguish infection regions from normal higher-density structures; and prospective clinical validation. Whether the underlying methodology extends to other medical imaging problems involving low-contrast structures is an open question that would require dedicated evaluation on the relevant modality and task and is not established by the present study.

5. Limitations

The lung-field ROI extraction introduced in this revision uses a convex hull of each thresholded lung component rather than a tight anatomical boundary. This is a deliberate design choice: a strict air-intensity mask would exclude ground-glass opacity and consolidation regions, which are denser and therefore brighter than normally aerated lung tissue, directly removing the pathology the framework is intended to detect. As a consequence, the mask retains a small margin of non-pulmonary tissue near the

lung border in some slices. In addition, the border-connected-component removal step, tuned for axial slices, occasionally clips lung regions that intersect the image boundary in coronal or sagittal views (e.g., near the apex); view-specific adjustment of this step is left for future work. Extension to a learned or contour-based lung segmentation model and validation of the ROI extraction step itself against expert-annotated lung boundaries are also identified as directions for future refinement. Scanner acquisition parameters were not available for the images used in this study, limiting the ability to assess how acquisition protocol variation may have influenced the reported results. Future evaluation using source DICOM data with complete acquisition metadata would strengthen reproducibility and allow assessment of generalizability across scanner types and imaging protocols.

As ground-glass opacity and consolidation are nonspecific radiological findings shared with other pulmonary conditions, the proposed method identifies regions of suspicious pulmonary abnormality rather than confirming COVID-19 infection specifically. Definitive diagnosis requires integration with clinical history, laboratory or virological testing, and radiologist interpretation; the proposed framework is intended as a supportive tool for imaging characterization and quantification, not as a standalone diagnostic system. The present evaluation is computational rather than clinical: quantitative performance was assessed against expert-annotated reference masks on a ten-image dataset, without radiologist review of the proposed method's outputs, comparison within an actual clinical workflow, or evaluation across a larger and more demographically diverse patient population. References to computational speed describe processing time only and should not be interpreted as a validated claim of clinical utility for rapid assessment. The area-gradient threshold criterion does not incorporate anatomical priors distinguishing pathological tissue from normal higher-density structures such as vasculature and bronchial walls. Reported segmentation accuracy (Table 6) reflects overall agreement with expert-annotated infection masks but does not isolate the specific contribution of vascular/bronchial inclusion to segmentation error. A structure-aware error analysis, potentially incorporating vessel-segmentation as an explicit exclusion step, is recommended for future work. Reference mask reliability depends on the annotation protocol of the source dataset, which is described only at the level of annotator qualifications and review stages rather than a fully published, detailed labeling protocol. Inter-annotator agreement statistics for the specific ten images used in this study are not available. This limits the extent to which the reliability of the reported Dice and IoU values can be independently assessed beyond the annotator-qualification information provided by the dataset source.

The reported quantitative results are based on ten CT images, which limits the statistical reliability of the performance estimates and their generalizability to broader patient populations, imaging protocols, and disease severity ranges. With this sample size, individual images can disproportionately influence the reported mean and variance, and the reported metrics should be interpreted as a preliminary, indicative assessment rather than a statistically robust estimate of population-level performance. Confidence intervals were not computed due to the limited sample size; a larger evaluation cohort would be required to support formal statistical inference, such as confidence intervals or hypothesis testing comparing methods.

Several constants in the enhancement pipeline—the Gaussian smoothing kernel size and σ (Equation (6)) and the run-length thresholds used for peak detection—were set empirically rather than derived analytically or learned from data. Design parameters for the enhancement stage, including the Gaussian smoothing standard deviation, were originally selected via informal inspection on the same dataset used for quantitative evaluation, rather than on an independent development set. While the sensitivity analysis in Table 1 shows the reported results are not sensitive to this specific value within a broad tested range, mitigating the risk of overfitting to the evaluation set, independent parameter selection on a separate dataset—followed by evaluation on a held-out test set—would provide stronger methodological assurance and is recommended for future work. These values were held fixed across all ten images in the test set rather than tuned individually per image. While this reflects a design limitation in that the constants were not derived from first principles, it also demonstrates that the reported results were not obtained by per-image parameter optimization: the same fixed configuration performs consistently across the full image set, indicating that the method's outputs are not overfit to individual cases. Analytical derivation or data-driven selection of these constants is identified as a direction for future work. Lung-field extraction was performed on rendered grayscale pixel intensity rather than calibrated Hounsfield Units, since the source images were obtained as rendered CT slices rather than raw DICOM volumes. This may reduce robustness across images with differing window/level settings compared to HU-based thresholding and is identified as an area for improvement in future work using source DICOM data. Preprocessing in this study was constrained by the nature of the available source data: because images were obtained as pre-windowed, rendered case images rather than raw DICOM data, CT windowing could not be independently standardized across the dataset, and no dedicated image-domain denoising step was applied. The framework's 2D, per-slice processing does not exploit inter-slice spatial context available in full CT volumes, which may limit performance relative to 3D-aware approaches. Future work using source DICOM volumes would enable standardized windowing, explicit denoising, and evaluation of 3D-aware extensions of the proposed framework. As illustrated in Figure 6, the lung-field extraction step can fail on individual images with atypical lung geometry, producing a mask that excludes peripheral lung tissue and propagating this error into the final segmentation. This failure mode was identified through visual inspection rather than systematic per-case validation, and its frequency across a larger dataset is not established by the present study.

Acknowledgment

The authors sincerely thank the editors and anonymous reviewers for their insightful comments and constructive feedback, which have significantly contributed to improving the quality and clarity of this work.

Funding Support

This research did not receive any specific grant from funding agencies in the public, commercial, or not-for-profit sectors.

Ethical Statement

This study did not involve the collection of new human or animal data by the authors. The chest CT images analyzed were obtained from a publicly available, de-identified dataset (the COVID-19 CT Lung and Infection Segmentation Dataset

[26]), assembled from cases originally shared via Radiopaedia.org under the data-sharing and consent terms of the contributing institutions; no additional ethical approval was required for this secondary, retrospective use of de-identified imaging data.

Conflicts of Interest

The authors declare that they have no known competing financial interests or personal relationships that could have appeared to influence the work reported in this paper.

Data Availability Statement

The CT images and expert-annotated reference masks used in this study are publicly available as part of the COVID-19 CT Lung and Infection Segmentation Dataset [26] at https://doi.org/10.5281/zenodo.3757476.

Author Contribution Statement

Debasish Biswas: Methodology, Software, Formal analysis, Investigation, Data curation, Visualization. **Shouvik Chakraborty**: Conceptualization, Methodology, Software, Formal analysis, Investigation, Resources, Data curation, Writing – original draft, Writing – review & editing, Visualization, Supervision, Project administration. **Chinmoy Ghorai**: Validation, Formal analysis, Data curation, Visualization, Supervision, Project administration.

References

[1] Isensee, F., Jaeger, P. F., Kohl, S. A. A., Petersen, J., & Maier-Hein, K. H. (2021). nnU-Net: A self-configuring method for deep learning-based biomedical image segmentation. *Nature Methods*, *18*(2), 203–211. https://doi.org/10.1038/s41592-020-01008-z

[2] Satushe, V., Vyas, V., Metkar, S., & Singh, D. P. (2025). AI in MRI brain tumor diagnosis: A systematic review of machine learning and deep learning advances (2010–2025). *Chemometrics and Intelligent Laboratory Systems*, *263*, 105414. https://doi.org/10.1016/j.chemolab.2025.105414

[3] Oulefki, A., Agaian, S., Trongtirakul, T., & Kassah Laouar, A. (2021). Automatic COVID-19 lung infected region segmentation and measurement using CT-scans images. *Pattern Recognition*, *114*, 107747. https://doi.org/10.1016/j.patcog.2020.107747

[4] Chen, H., Jiang, Y., Loew, M., & Ko, H. (2022). Unsupervised domain adaptation based COVID-19 CT infection segmentation network. *Applied Intelligence*, *52*(6), 6340–6353. https://doi.org/10.1007/s10489-021-02691-x

[5] Dey, S., Kundu, B., Basuchowdhuri, P., Saha, S. K., & Chakraborti, T. (2024). A fast domain-inspired unsupervised method to compute COVID-19 severity scores from lung CT. In *International Conference on Pattern Recognition*, 60–74. https://doi.org/10.1007/978-3-031-78198-8_5

[6] Sahaya Pushpa Sarmila Star, C., Inbamalar, T. M., & Milton, A. (2025). Segmentation of breast lesion using fuzzy thresholding and deep learning. *Computers in Biology and Medicine*, *184*, 109406. https://doi.org/10.1016/j.compbiomed.2024.109406

[7] Zheng, Y., Xu, Z., & Wang, X. (2022). The fusion of deep learning and fuzzy systems: A state-of-the-art survey. *IEEE Transactions on Fuzzy Systems*, *30*(8), 2783–2799. https://doi.org/10.1109/TFUZZ.2021.3062899

[8] Bhakta, R., & Hossain, A. B. M. A. (2020). Lung tumor segmentation and staging from CT images using fast and robust fuzzy c-means clustering. *International Journal of Image, Graphics and Signal Processing*, *12*(1), 38–45. https://doi.org/10.5815/ijigsp.2020.01.05

[9] Nithisha, J., Visumathi, J., Rajalakshmi, R., Suseela, D., Sudha, V., Choubey, A., & Farhaoui, Y. (2025). Fuzzy hybrid meta-optimized learning-based medical image segmentation system for enhanced diagnosis. *International Journal of Information Technology and Computer Science*, *17*(1), 47–66. https://doi.org/10.5815/ijitcs.2025.01.04

[10] Nia, S. N., & Shih, F. Y. (2024). Medical X-ray image enhancement using global contrast-limited adaptive histogram equalization. *International Journal of Pattern Recognition and Artificial Intelligence*, *38*(12), 2457010. https://doi.org/10.1142/S0218001424570106

[11] Najafi, H., Savoji, K., Mirzaeibonehkhater, M., Moravvej, S. V., Alizadehsani, R., & Pedrammehr, S. (2024). A novel method for 3D lung tumor reconstruction using generative models. *Diagnostics*, *14*(22), 2604. https://doi.org/10.3390/diagnostics14222604

[12] Vilone, G., & Longo, L. (2021). A quantitative evaluation of global, rule-based explanations of post-hoc, model agnostic methods. *Frontiers in Artificial Intelligence*, *4*, 717899. https://doi.org/10.3389/frai.2021.717899

[13] Chakraborty, S., Mali, K., & Mitra, S. (2024). Affinity propagation in semi-supervised segmentation: A biomedical application. *IEEE Transactions on Systems, Man, and Cybernetics: Systems*, *54*(10), 6023–6032. https://doi.org/10.1109/TSMC.2024.3416268

[14] Barcelos, I. B., Belem, F. D. C., Joao, L. D. M., Patrocínio, Z. K. D., Jr., Falcao, A. X., & Guimarães, S. J. F. (2024). A comprehensive review and new taxonomy on superpixel segmentation. *ACM Computing Surveys*, *56*(8), 1–39. https://doi.org/10.1145/3652509

[15] Zhao, X., & Xu, W. (2024). NFMPAtt-UNet: Neighborhood fuzzy c-means multi-scale pyramid hybrid attention unet for medical image segmentation. *Neural Networks*, *178*, 106489. https://doi.org/10.1016/j.neunet.2024.106489

[16] Ibrahim, H., & Pik Kong, N. (2007). Brightness preserving dynamic histogram equalization for image contrast enhancement. *IEEE Transactions on Consumer Electronics*, *53*(4), 1752–1758. https://doi.org/10.1109/TCE.2007.4429280

[17] Javanmard, Z., Zarean Shahraki, S., Safari, K., Omidi, A., Raoufi, S., Rajabi, M., . . . , & Aria, M. (2025). Artificial intelligence in breast cancer survival prediction: A comprehensive systematic review and meta-analysis. *Frontiers in Oncology*, *14*, 1420328. https://doi.org/10.3389/fonc.2024.1420328

[18] Loftus, T. J., Shickel, B., Ruppert, M. M., Balch, J. A., Ozrazgat-Baslanti, T., Tighe, P. J., . . . , & Bihorac, A. (2022). Uncertainty-aware deep learning in healthcare: A scoping review. *PLOS Digital Health*, *1*(8), e0000085. https://doi.org/10.1371/journal.pdig.0000085

[19] Khayyat, M. M., Zamzami, N., Zhang, L., Nappi, M., & Umer, M. (2024). Fuzzy-CNN: Improving personal human identification based on IRIS recognition using LBP features. *Journal of Information Security and Applications*, *83*, 103761. https://doi.org/10.1016/j.jisa.2024.103761

[20] Savalia, M. R., & Verma, J. V. (2023). Classifying malignant and benign tumors of breast cancer: A comparative

investigation using machine learning techniques. *International Journal of Reliable and Quality E-Healthcare*, *12*(1), 1–19. https://doi.org/10.4018/IJRQEH.318483

[21] Lin, C. J., Chen, B. H., Lin, C. H., & Jhang, J. Y. (2024). Design of a convolutional neural network with type-2 fuzzy-based pooling for vehicle recognition. *Mathematics*, *12*(24), 3885. https://doi.org/10.3390/math12243885

[22] Yao, W., Bai, J., Liao, W., Chen, Y., Liu, M., & Xie, Y. (2024). From CNN to transformer: A review of medical image segmentation models. *Journal of Imaging Informatics in Medicine*, *37*(4), 1529–1547. https://doi.org/10.1007/s10278-024-00981-7

[23] Mustafa, W. A. W., Khiruddin, K., Jamaludin, K. R., Khusairi, F. Y., & Ismail, S. (2025). Comparative analysis of cervical cell classification using machine learning algorithms. *Journal of Electronics, Electromedical Engineering, and Medical Informatics*, *7*(3), 646–662. https://doi.org/10.35882/jeeemi.v7i2.652

[24] Wang, Y., Wang, H., Shen, Y., Fei, J., Li, W., Jin, G., . . . , & Le, X. (2022). Semi-supervised semantic segmentation using unreliable pseudo-labels. In *2022 IEEE/CVF Conference on Computer Vision and Pattern Recognition (CVPR)*, 4238–4247. https://doi.org/10.1109/CVPR52688.2022.00421

[25] Chakraborty, S., & Mali, K. (2024). A multilevel biomedical image thresholding approach using the chaotic modified cuckoo search. *Soft Computing*, *28*(6), 5359–5436. https://doi.org/10.1007/s00500-023-09283-6

[26] Ma, J., Wang, Y., An, X., Ge, C., Yu, Z., Chen, J., . . . , & Yang, X. (2021). Toward data-efficient learning: A benchmark for COVID-19 CT lung and infection segmentation. *Medical Physics*, *48*(3), 1197–1210. https://doi.org/10.1002/mp.14676

[27] Müller, D., Soto-Rey, I., & Kramer, F. (2021). Robust chest CT image segmentation of COVID-19 lung infection based on limited data. *Informatics in Medicine Unlocked*, *25*, 100681. https://doi.org/10.1016/j.imu.2021.100681

[28] Jaffar, M. A., Hussain, A., Nazir, M., Mirza, A. M., & Chaudhry, A. (2008). GA and morphology based automated segmentation of lungs from CT scan images. In *2008 International Conference on Computational Intelligence for Modelling Control & Automation*, 265–270. https://doi.org/10.1109/CIMCA.2008.168

[29] Liu, J., Wang, Z., & Zhang, R. (2009). Liver cancer CT image segmentation methods based on watershed algorithm. In *I2009 International Conference on Computational Intelligence and Software Engineering*, 1–4. https://doi.org/10.1109/CISE.2009.5364437

[30] Fan, D.-P., Zhou, T., Ji, G.-P., Zhou, Y., Chen, G., Fu, H., . . . , & Shao, L. (2020). Inf-Net: Automatic COVID-19 lung infection segmentation from CT images. *IEEE Transactions on Medical Imaging*, *39*(8), 2626–2637. https://doi.org/10.1109/TMI.2020.2996645

How to Cite: Biswas, D., Chakraborty, S., & Ghorai, C. (2026). A Fuzzy Morphological Approach for Unsupervised Lung Infection Segmentation in Chest CT Images. *Medinformatics*. https://doi.org/10.47852/bonviewMEDIN620210434